

# A survey of methane point source emissions from coal mines in Shanxi province of China using AHSI on board Gaofen-5B

Zhonghua He<sup>1</sup>, Ling Gao<sup>2</sup>, Miao Liang<sup>3</sup>, Zhao-Cheng Zeng<sup>4,\*</sup>

<sup>1</sup>Zhejiang Climate Centre, Zhejiang Meteorological Bureau, Hangzhou, 310052, China

5 <sup>2</sup>National Satellite Meteorological Centre, China Meteorological Administration, Beijing 100081, China

<sup>3</sup>Meteorological Observation Centre, China Meteorological Administration, Beijing, 100081, China

<sup>4</sup>Institute of Remote Sensing and GIS, School of Earth and Space Sciences, Peking University, Beijing, 100871, China

*Correspondence to: Z.-C. Zeng (zczeng@pku.edu.cn)*

**Abstract.** Satellite-based detection of methane (CH<sub>4</sub>) point sources is crucial in identifying and mitigating anthropogenic emissions of CH<sub>4</sub>, a potent greenhouse gas. Previous studies have indicated the presence of CH<sub>4</sub> point source emissions from coal mines in Shanxi, China, an important source region with large CH<sub>4</sub> emissions, but a comprehensive survey has remained elusive. This study aims to conduct a survey of CH<sub>4</sub> point sources over Shanxi's coal mines based on observations of the Advanced HyperSpectral Imager (AHSI) on board the Gaofen-5B satellite (GF-5B/AHSI) between 2021 and 2023. The spectral shift in center wavelength and change in full-width-half-maximum (FWHM) from the nominal design values are estimated for all spectral channels, which are used as inputs for retrieving the enhancement of column-averaged dry-air mole fraction of CH<sub>4</sub> ( $\Delta X_{CH_4}$ ) using a matched-filter based algorithm. Our results show that the spectral calibration on GF-5B/AHSI reduced estimation biases of emission flux rate by up to 5.0%. We applied the flood-fill algorithm to automatically extract emission plumes from  $\Delta X_{CH_4}$  maps. We adopted the integrated mass enhancement (IME) model to estimate the emission flux rate values from each CH<sub>4</sub> point source. Consequently, we detected CH<sub>4</sub> point sources in 32 coal mines with 93 plume events in Shanxi province. The estimated emission flux rate ranges from  $761.78 \pm 185.00 \text{ kg}\cdot\text{h}^{-1}$  to  $12729.12 \pm 4658.13 \text{ kg}\cdot\text{h}^{-1}$ . Our results show that wind speed is the dominant source of uncertainty contributing about 84.84% to the total uncertainty in emission flux rate estimation. Interestingly, we found a number of false positive detections due to solar panels that are widely spread in Shanxi. This study also evaluates the accuracy of wind fields in ECMWF ERA5 reanalysis by comparing with ground-based meteorological station. We found large discrepancy, especially in wind direction, suggesting incorporating local meteorological measurements into the study CH<sub>4</sub> point source are important to achieve high accuracy. The study demonstrates that GF-5B/AHSI possesses capabilities for monitoring large CH<sub>4</sub> point sources over complex surface characteristics in Shanxi.

## 1 Introduction

30 Due to its potent radiative forcing and relatively short lifespan of about a decade, methane (CH<sub>4</sub>), the second most significant anthropogenic greenhouse gas after atmospheric carbon dioxide, is an effective target that attracts increasing attention for emission reduction and climate change mitigation (IPCC, 2021). Human activity related sources of atmospheric CH<sub>4</sub> primarily include agricultural activities like livestock farming and rice cultivation, industrial processes such as petroleum, natural gas, and coal extraction, as well as landfills and waste management (Lu et al., 2022). Among these, industrial activities related to fossil fuel production contribute nearly 35% of global anthropogenic CH<sub>4</sub> emissions (Saunois et al., 2020), not only triggering the greenhouse effect but also leading to significant energy wastage (Chen et al., 2023). Methane emissions escaping from energy production activities primarily stem from industrial infrastructure emissions, such as wells, collection and compression stations, storage tanks, pipelines, and processing plants, easily forming "point sources" of CH<sub>4</sub> emissions (Varon et al., 2019). With the destruction of geological processes involved in mining activities, the release of coalbed methane captured in coal seams and surrounding rock strata forms the point source of CH<sub>4</sub> emission from coal mines (Zheng et al., 2019). These emissions plumes of gas release from point sources contain high concentrations of CH<sub>4</sub> over relatively small surface areas (Duren et al., 2019). The overall plumes formed by point source emissions exhibit a notable heavy-tailed distribution (Irakulis-Loitxate et al., 2021). However, due to the comprehensive effect of emission magnitude, land cover types, wind speed and direction, these plumes often show different characteristics across different time and space changes (Sánchez-García et al., 2022), which makes the plume detection and emission estimation challenging. Given that such emissions contribute significantly to regional CH<sub>4</sub> emissions (Frankenberg et al., 2016), it is important to have accurate detection and estimation. As atmospheric CH<sub>4</sub> is colourless and odourless, coupled with the strong uncertainty in the temporal and spatial distribution of point source emissions, satellite remote sensing using high resolution spectroscopy has become a crucial means for detecting CH<sub>4</sub> point source emissions due to its high sensitivity, wide coverage and high revisit capabilities (Pandey et al., 2021).

Satellite observations for detecting global atmospheric CH<sub>4</sub> concentrations with high spatiotemporal resolution, provides data support for accounting and assessing reduction measures (Jacob et al., 2022). Satellite detection and quantification of CH<sub>4</sub> super-emitters was first demonstrated in the 2015 Aliso Canyon blowout incident using the Hyperion imaging spectrometer on board EO-1 (Thompson et al., 2016). Satellites with high spatial resolution but with moderate spectral resolution have successfully detected and traced CH<sub>4</sub> point source emissions. The currently in orbit satellites include GHGSat operated by a private company in Canada (2016-present; Jervis et al., 2021), Italy's PRISMA (2019-present; Guanter et al., 2021), China's GF-5 and ZY-1 satellites (Irakulis-Loitxate et al., 2021), NASA's EMIT (Thorpe et al., 2023), and the German EnMAP mission (Guanter et al., 2015). While multispectral (Landsat-8/9, Sentinel-2, and WorldView-3) and coarse-resolution high-spectral satellites (Sentinel-5P TROPOMI) have also been widely validated for detecting extra-large CH<sub>4</sub> plumes (Ehret et al., 2022; Varon et al., 2021; Sanchez-Garcia et al., 2022; Lauvaux et al., 2022), limitations in spectral or spatial resolution result in differences in detection sensitivity, estimation uncertainty, and tracing capabilities. The first generation AHSI on

board China's GF-5A (GF-5A/AHSI) exhibits high capabilities in detecting CH<sub>4</sub> point source emissions. As shown in **Irakulis-Loitxate et al. (2021)**, 37 unexpected emission point sources exceeding 500 kg·h<sup>-1</sup> can be identified in the Permian Basin oil and gas fields using a total of 30 images from GF-5A and PRISMA satellites during several days in 2019 and 2020, illustrating the potential of AHSI in regional CH<sub>4</sub> point source survey. To estimate emissions from CH<sub>4</sub> point source, these studies typically employ spectral matching filtering method to derive CH<sub>4</sub> increment ( $\Delta X_{CH_4}$ ) and then estimate flux rate using integrated mass enhancement (IME) model (**Varon et al., 2018**). These studies have previously provided available techniques in the identification of point sources in local or national scales (e.g., Algeria, Permian, China, USA), and flux estimation and uncertainty analyses for these point sources (**Guanter et al., 2021; Irakulis-Loitxate et al., 2021**).

As the world's largest coal producer, China contributes 50.7% of the global coal production in 2020, making it one of the largest emitters of CH<sub>4</sub> from coal mining (**Chen et al., 2022b**), especially in Shanxi province, where most underground coal mines are located (**Qin et al., 2023**). However, due to the influence of complex surface conditions on the background spectral characteristics, satellite observations exhibit notably lower sensitivity in the detection of CH<sub>4</sub> point source emissions in Shanxi compared to other regions with more homogeneous land surfaces (**Sánchez-García et al., 2022; Guanter et al., 2021**). In addition, the wind fields from reanalysis datasets may be subject to high uncertainty due to the complex terrain in Shanxi, leading to highly uncertain emission flux rate estimation (**Jongaramrungruang et al., 2021**). Although TROPOMI imagery and convolutional neural networks have been shown to effectively detect potential large CH<sub>4</sub> emission point sources globally (**Schuit et al., 2023**), the specific localization and tracing of CH<sub>4</sub> emission point sources in China remain difficult due to the limitations of coarse spatial resolution and complex regional backgrounds, warranting further surveying efforts.

This study aims to conduct a survey of the CH<sub>4</sub> point source plumes in Shanxi by developing a framework to detect and estimate emissions flux rate using the latest hyperspectral observations from GF-5B/AHSI from 2021 to 2023. Specifically, this study focuses on (1) quantifying the impact of the shift in spectral wavelength and the change in spectral instrument line shape (ILS) from the nominal design values for the spectral channels of GF-5/AHSI on CH<sub>4</sub> retrieval and emission estimation; (2) Identifying CH<sub>4</sub> point source plumes using the matched filter method; (3) automating the segmentation of emission plumes from the retrieved CH<sub>4</sub> enhancement maps; (4) Estimating emissions flux rate from point sources using IME method; (5) Understanding the spatial and temporal patterns of CH<sub>4</sub> emissions from point sources in Shanxi.

## 2 Study area and used datasets

### 2.1 Study area

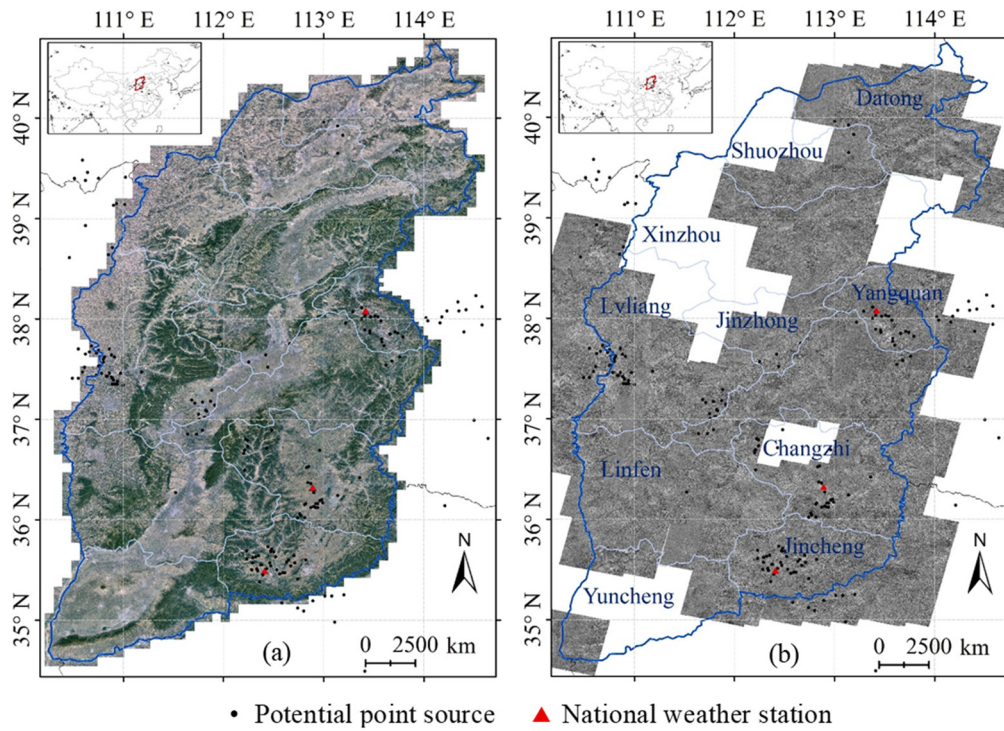
Shanxi Province is the most extensively mined region in China, harbouring nearly half of the nation's suspected point sources based on TROPOMI observations (**Schuit et al., 2023**). It stands as a typical area for CH<sub>4</sub> point source emissions in China and has been a focal point in prior comparative studies on point source emissions (**Sanchez-Garcia et al., 2022; Guanter et al., 2021**). Shanxi Province (**Figure 1**), situated in northern China, experiences a temperate continental monsoon climate

characterized by cold, dry winters and hot, humid summers. The region boasts diverse topography, comprising mountains, plateaus, and basins. Consequently, the stable atmospheric conditions during winter can lead to the accumulation of pollutants closer to the ground, impacting the detection of CH<sub>4</sub> emissions. Although the region has strict rules in regulating the process of CH<sub>4</sub>, a by-product of coal mining, underground coal mines in Shanxi releases CH<sub>4</sub> to the atmosphere from mine venting. Therefore, the identification of these plumes will help mitigate CH<sub>4</sub> emissions over this region.

## 2.2 GF-5B/AHSI dataset

The GF-5B satellite is the 2<sup>nd</sup> satellite of the Gaofen-5 series and was launched on September 7, 2021. It has accumulated over two years' worth of global observational data to date. Equipped with the Advanced Hyperspectral Imager (AHSI), it can capture spectral information spanning 400 to 2500 nm with a spatial resolution of 30 meters over a 60 km swath, encompassing 330 spectral channels with spectral resolutions of 5 and 10 nm in the VNIR and SWIR, respectively (Liu et al., 2019). Its relatively high signal-to-noise ratio (around 500 in the Short-Wave Infrared, SWIR) presents notable advantages in detecting CH<sub>4</sub> point source emissions (Irakulis-Loitxate et al., 2021). The retrieval of the enhancement of column-averaged dry-air mole fraction of CH<sub>4</sub> ( $\Delta XCH_4$ ) relies primarily on strong CH<sub>4</sub> absorption features near 2300 nm, while the 2100 to 2450 nm spectral window of the GF-5B/AHSI demonstrates higher sensitivity to XCH<sub>4</sub> variations, thereby possessing enhanced capabilities for precise CH<sub>4</sub> concentration inversion. This study focuses on Shanxi Province, using images from 111 GF-5B/AHSI scenes covering suspected point sources from September 2021 to September 2023, with a cloud cover of less than 10%, employed for  $\Delta XCH_4$  inversion and point source identification (Figure 1b). These images cover the major emission hotspots as identified by TROPOMI data (Schuit et al., 2023). Noted that, in Shanxi, the overpassing time of GF-5/AHSI is around 11-12 Beijing Time (BJT).





115 **Figure 1. (a) The study area in Shanxi enclosed by the blue boundary with the background image from © Google Maps, and (b) Gaofen-5B observed scene images used for the CH<sub>4</sub> plume survey. The black dots represent the potential point sources detected by TROPOMI (Schuit et al., 2023). The red dots represent the three national weather stations for monitoring meteorological variables in Yangquan, Changzhi, and Jincheng used for wind fields comparison with ERA5 reanalysis (Section 4.3).**

### 2.3 Auxiliary data

120 Methane point source detection and emission estimation involve various auxiliary datasets, mainly including: (1) Ultra-high-resolution surface imagery for checking false positive in point source detection; (2) Wind fields information for estimate emissions from point source plumes; (3) Digital Elevation Model (DEM) data for the geometric correction of AHSI imagery. High-resolution surface imagery is an indispensable dataset in point source identification and serves as direct evidence for distinguishing interference signals. The high-resolution imagery used in this study primarily comes from Google Earth. Wind

125 speed data is a critical parameter for calculating emission flux rates. The study utilized U<sub>10</sub> hourly wind speed reanalysis products from ECMWF ERA5, with a spatial resolution of 0.25x0.25 degrees (Muñoz-Sabater et al., 2021). Terrain data is crucial for the geometric correction of AHSI imagery, directly impacting the positioning and identification of ΔXCH<sub>4</sub> plume signals. The study used DEM data from STRM (Farr et al., 2007), with a spatial resolution of 30 meters. Additionally, the study obtained hourly meteorology monitoring data, including wind speed and wind direction, from January 2021 to September

130 2023 from three national meteorological stations in Yangquan, Changzhi, and Jincheng (Figure 1), obtained from the China

Meteorological Administration Data Centre. These data were compared with ERA5's  $U_{10}$  hourly wind speed reanalysis products to investigate the uncertainty of the ERA5's wind field.

### 3 Methods

135 The retrieval of  $\Delta XCH_4$  and estimation of emission flux rate from high-resolution hyperspectral data have been implemented in many previous studies (e.g., **Cusworth et al., 2020; Guanter et al., 2021; Huang et al., 2020; Varon et al., 2018; Frankenberg et al., 2016**) using a combination of matched filter method and the IME model. This study primarily applies this combined approach to survey the  $CH_4$  point source emissions in Shanxi using GF-5B/AHSI. In addition, this study focuses on the quantification the impact of the spectral shift and the change in spectral ILS on the point source emission estimation, the automation of the segmentation of emission plumes from the retrieved  $CH_4$  enhancement maps, and the analysis of the spatial and temporal patterns of  $CH_4$  emissions from point sources in Shanxi.  
140

#### 3.1 $\Delta XCH_4$ retrieval using matched filter method

##### 3.1.1 Spectral calibration of GF-5B/AHSI

Spectral shift of centre wavelength and change in FWHM relative to the nominal spectral calibration for spectral channels significantly affects the retrieval results of  $\Delta XCH_4$  using spectral matched filter method (e.g., **Guanter et al., 2021**). The spectral shift and FWHM change vary distinctly between different image scenes. It is therefore important to re-calibrate the spectra for all channels before further analysis using the observed spectra. While GF-5B AHSI imagery has been utilized in  $CH_4$  point source detection experiments in various regions, estimation regarding its spectral offset and associated correction in FWHM have not yet been undertaken. In this study, we conduct this spectral calibration for the Short-Wave Infrared (SWIR) channels from 2110 nm to 2455 nm of GF-5B/AHSI data (**Guanter et al., 2009**). The basic idea of the spectral calibration is to retrieve the wavelength shift and FWHM change that would lead to the best fit between observed GF-5B/AHSI spectra and the simulated spectra based on radiative transfer model. In practice, we used the forward radiative transfer model and optimal estimation method in GFIT3 (**Zeng et al., 2021**) to iteratively derive the spectral calibration parameters. Similar to **Guanter et al. (2021)**, we applied the calibration to the averaged top-of-the-atmosphere radiance from all observations of each across-track detector and derive the wavelength shift and FWHM change. This calibration is repeated for all detectors and over all GF-5B/AHSI images. Eventually, the updated spectral centre wavelength and FWHM, replacing the nominal values, for all channels are used as inputs in the  $\Delta XCH_4$  retrieval when the high-resolution  $CH_4$  absorption spectra is convolved with Gaussian ILS.  
150  
155

### 3.1.2 Spectral matched filter for retrieving $\Delta XCH_4$

Spectral matched filter method derives the  $\Delta XCH_4$  by calculating the difference between the “polluted” spectra over a source region with background spectra of the ambient atmosphere, and expressing the difference by the number of target absorption spectrum from one unit of  $XCH_4$  (e.g., 1 ppm of  $XCH_4$ ; **Guanter et al., 2021**). The retrieval using matched filter is depicted in **Equation (1)**:

$$\Delta XCH_4 = ((\mathbf{x} - \boldsymbol{\mu})^T \boldsymbol{\Sigma}^{-1} \mathbf{t}) / (\mathbf{t}^T \boldsymbol{\Sigma}^{-1} \mathbf{t}) \quad (1)$$

Where,  $\mathbf{x}$  denotes a vector of the observed SWIR hyperspectral spectra from a target pixel. In this study, the  $CH_4$  strong absorption band (2110-2455 nm) is used;  $\boldsymbol{\mu}$  and  $\boldsymbol{\Sigma}$  represent the mean and covariance of the SWIR hyperspectral observation over background regions, respectively.  $\mathbf{t}$  is target spectrum, representing the disturbance vector of SWIR hyperspectral due to enhanced  $XCH_4$  relative to the background. It can be derived from an element-wise multiplication of  $\boldsymbol{\mu}$  and the unit  $XCH_4$  absorption spectrum  $\boldsymbol{\kappa}$ , which is generated from GFIT3 (**Zeng et al., 2021**), as shown in **Figure 2**, assuming a perturbation of 1 ppm  $XCH_4$ .

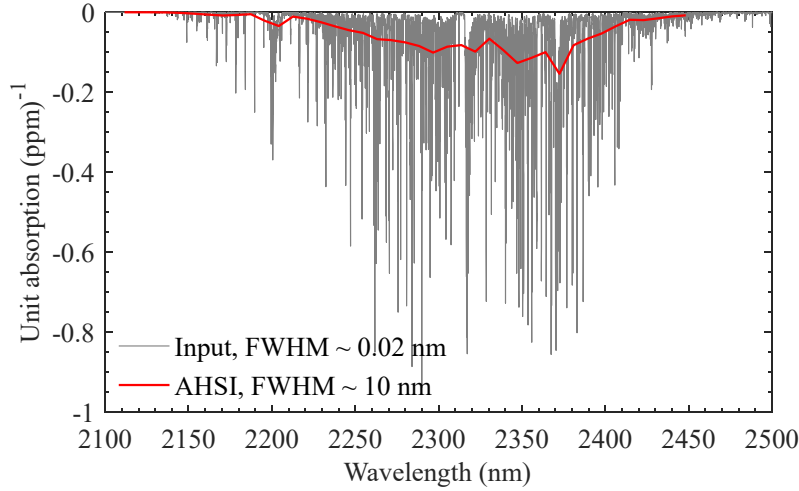


**Figure 2.** Example of unit  $XCH_4$  absorption spectrum used as target signature in the matched filter retrieval method. The high-resolution target signature (in grey) represents absorptivity induced by 1 ppm  $XCH_4$  enhancement, which is calculated using GFIT3 (**Zeng et al., 2021**). The high-resolution absorptions are then convolved with a Gaussian ILS with nominal FWHM from GF-5B/AHSI to derive the spectra (in red) that can be compared with observed from AHSI.

### 3.2 Identifying point source plumes from $\Delta XCH_4$ maps

After data pre-processing, including spectral re-calibration and  $\Delta XCH_4$  retrieval, we implemented a geometric localization to change the GF-5B/AHSI imagery index for row and column pixels to latitude and longitude under WGS84 projection. The detailed description of this geometric localization is in the **Appendix A**. Then, this study compares the  $\Delta XCH_4$  maps with high-resolution Google Earth imagery to visually inspect and preliminarily identify the  $CH_4$  point source plumes. The identification criteria include: (1) high  $\Delta XCH_4$  values displaying plume characteristics; (2) the presence of ground facilities such as factories or pipelines representing potential  $CH_4$  emission sources; (3) plume distribution characteristics not caused by

terrain features that may impact short-wave infrared strong absorption in surface features. Although wind conditions directly affect plume features, however, reanalysis data (e.g., ERA5) of wind direction may be very different from the plume structure. Several factors could contribute to this mismatch, including the temporal and spatial resolution of the reanalysis data, local topographical features, and microscale meteorological phenomena that are not fully captured by the reanalysis data. Therefore, this study temporarily refrains from utilizing wind direction from ERA5 reanalysis as a direct criterion for point source identification.

### 3.3 Estimation of emission flux rates

#### 3.3.1 Automatic segmentation of $\Delta XCH_4$ plumes using flood-fill algorithm

The segmentation of  $\Delta XCH_4$  plumes in previous studies have often been manually drawn, a laborious and time-consuming process highly influenced by subjective human judgment, leading to possible bias in IME calculations. Hence, there's a need to introduce a statistically-based, relatively objective, and easy to implement method for  $\Delta XCH_4$  plume segmentation. The flood-fill algorithm has been widely employed for segmenting and extracting continuous abnormal signals (He et al., 2018; Zscheischler et al., 2013), showing potential for  $\Delta XCH_4$  plume automatic segmentation. Specifically, this study uses statistical parameters, including  $\Delta XCH_4$  mean and one standard deviation, within the study area to segment and identify concentration-enhanced signals of  $\Delta XCH_4$ . It employs the flood-fill algorithm to recognize abnormal pixels in the vicinity of eight directions, merging spatially connected pixels into a plume pattern by considering the spatial continuity of plumes. To carry out the flood-fill method in plume extraction, a background region needs to be defined to calculate the mean and standard deviation of  $\Delta XCH_4$  which set the basis for identifying anomalous high  $\Delta XCH_4$  in the plume relative to the background. In this study, for a specific plume, the origin is first pinpointed through visual interpretation. Then a background region is defined as a square using the source origin as the center for calculating the mean ( $\mu$ ) and standard deviation ( $\sigma$ ) of  $\Delta XCH_4$ . Finally, a threshold defined based on  $\mu$  and  $\sigma$  is used for the flood-fill algorithm to effectively segment the point source plume. The exact numbers for the lengths of the background square and the defined thresholds are introduced in Section 3.3.3.

#### 3.3.2 Estimation of $CH_4$ point source emission flux rates

For emission flux rate estimation, this study employs the IME model (Equation (2); Frankenberg et al., 2016; Varon et al., 2018; Guanter et al., 2021) to calculate the excess mass of  $CH_4$  in the plumes relative to the background from the retrieved  $\Delta XCH_4$  plume maps. Then the emission flux rate ( $Q$ ) is calculated using Equation (3) with inputs of wind speed and the length of the plume. These equations are:

$$IME = k \sum_{i=1}^{n_p} \Delta XCH_4(i) \quad (2)$$

$$Q = ((\alpha \cdot U_{10} + \beta) \cdot IME) / L \quad (3)$$

where  $n_p$  denotes the number of pixels in the plume;  $\Delta XCH_4(i)$  represents the  $XCH_4$  enhancement in pixel  $i$ ;  $k$  is the scaling factor converting  $\Delta XCH_4$  from volume mixing ratio to mass based on Avogadro's law, considering the pixel resolution of GF-5B/AHSI to be 30-meter. In **Guanter et al. (2021)**,  $k$  is defined as  $5.155 \times 10^{-3} \text{ kg} \cdot \text{ppb}^{-1}$  derived from surface pressure of one standard atmosphere. However, the average elevation of the identified plumes in Shanxi is 942.41 meters (**Figure B1**), whose surface pressure (900.64 hPa on average) is about 10% less than one standard atmosphere. Therefore, we calculated a new  $k$  based on the derived averaged surface pressure for all the identified plumes. The derived  $k$  value ( $4.565 \times 10^{-3} \text{ kg} \cdot \text{ppb}^{-1}$ ) is then used for estimating IME in this study.  $Q$  denotes the point source emission rate, in unit of mass per unit time, obtained from IME calculation;  $(\alpha \cdot U_{10} + \beta)$  denotes the effective wind speed derived from wind speed at 10-meter from ERA5 reanalysis;  $L$  is the plume length, defined as the square root of the plume mask area (**Varon et al., 2018**).  $\alpha$  and  $\beta$  can be determined through Large Eddy Simulation based on the spatial resolution of satellite observation and  $\Delta XCH_4$  retrieval accuracy from GF-5B/AHSI. In this study, we adopted the estimates ( $\alpha=0.37$  and  $\beta=0.64$ ) from **Li et al. (2023)** derived for the Changzhi region in Shanxi. Globally, the values of  $\alpha$  and  $\beta$  do not change significantly. For example, the values adopted for PRISMA (**Gaunter et al., 2021; Irakulis-Loitxate et al., 2021**) were 0.34 and 0.44, and for GF-5B in the Permian basin (**Li et al., 2023**) were 0.38 and 0.41, respectively.

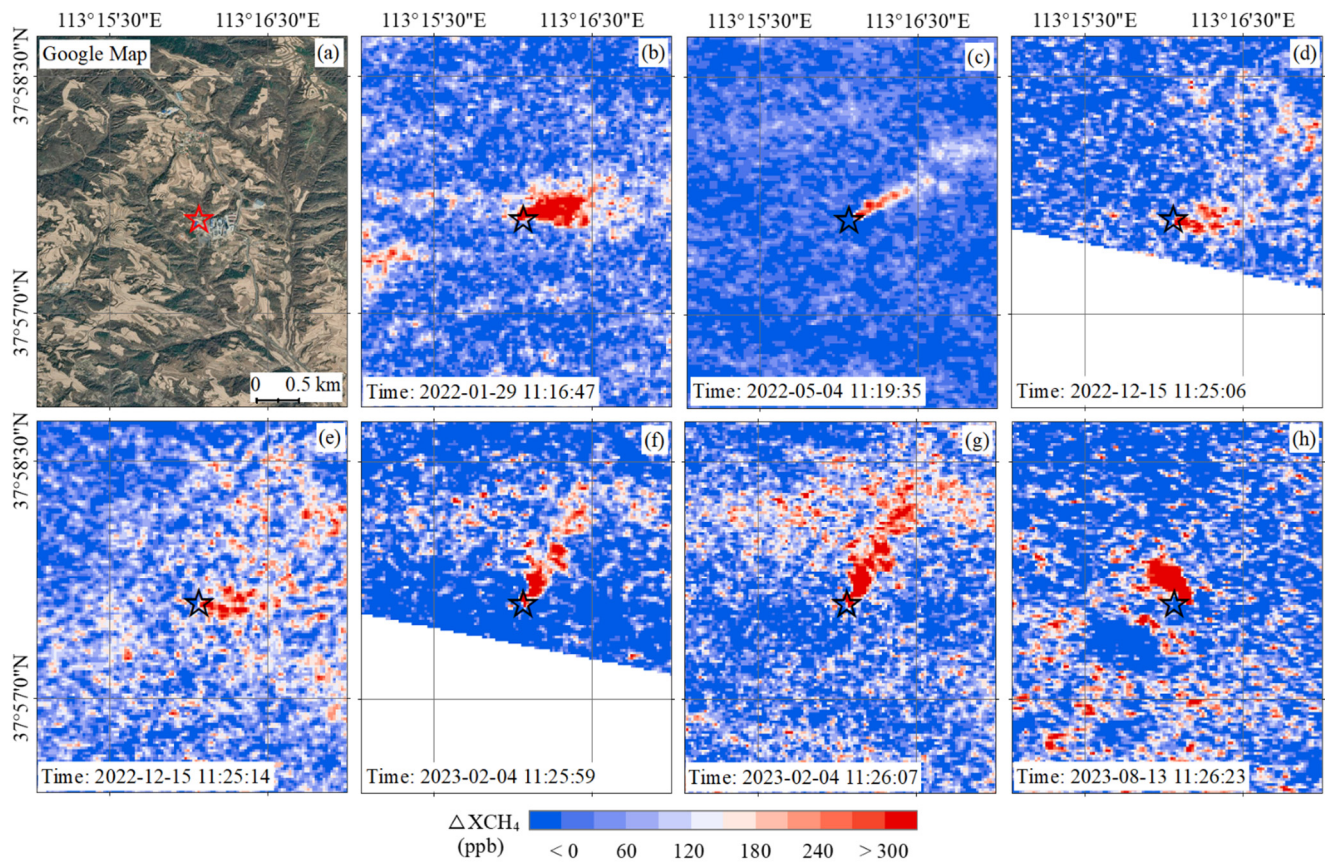
### 3.3.3 Estimation uncertainty of point source emission flux rate

The uncertainty of point source emission flux rate typically involves two primary aspects: the IME calculation and wind speed. For the IME calculation based on the statistically-driven method of flood-fill in plume extraction, the square background region and the threshold setting for plume enhancement segmentation are the main factors involved. Referring to the uncertainty assessment method by **Cusworth et al. (2020)**, we first assess the uncertainty of IME and then propagate the random errors of IME and wind speed ( $U_{10}$ ) to the flux rate  $Q$ , thereby evaluating the uncertainty of the estimated emission flux rate. In practice, for estimating IME and its uncertainty for a certain plume, we used 6 different lengths for the background square (from 12 km to 24 km with an interval of 2.4 km) and 6 different segmentation thresholds (from  $\mu+0.45\sigma$  to  $\mu+0.55\sigma$  with an interval of  $0.02\sigma$ ) for the flood-fill segmentation method (**Figure C1**). Different values of  $\mu$  and  $\sigma$  are calculated for different background regions. This process enabled the extraction of 36 reasonable plume values, defining their mean and standard deviation as the IME estimation and its uncertainty, respectively. For the wind speed uncertainty, to be consistent with the previous study, we set it at 50% for  $U_{10}$  (**Cusworth et al., 2020; Guanter et al., 2021**). To further understand the uncertainty of the used wind fields, in Section 4.3, we have carried out an evaluation of wind speeds and wind directions from ERA5 reanalysis by comparison with observations from meteorological sites in Shanxi.

#### 4.1 Detection and estimation of emission flux rate for single CH<sub>4</sub> point source using GF-5B/AHSI

**Figure 3** demonstrates the retrieval results of point sources  $\Delta XCH_4$  based on multiple capturing of the same point source using GF-5B/AHSI from January 2022 to August 2023. Under different emission flux rates and wind conditions, the emission plumes exhibited various characteristics. Six observations occurred during the winter-spring seasons (**Figure 3(b)-(g)**), showing  $\Delta XCH_4$  plumes spreading north-eastward, while the observation in summer (**Figure 3(h)**) displayed a plume drifting north-westward. An intriguing aspect is the occurrence of two repeated observations of the same point source within an 8-second interval (**Figure 3(d) and (e), Figure 3(f) and (g)**). The short revisit time of the same point source is a result of the special observation configuration of the SWIR imagery in the AHSI band, which employs a strategic arrangement of four strips. Each SWIR strip corresponds to a 15-km ground swath, resulting in a continuous 60 km swath width across the satellite orbit with 4 images combined. This configuration yields a total of 2,012 pixels (including 36 overlapped pixels) along the spatial dimension of the SWIR detectors (**Liu et al., 2019b**). Therefore, the target inside the overlapped pixels could be observed twice in 8 seconds. Theoretically, CH<sub>4</sub> emissions from the same point source within an 8-second interval should exhibit very similar patterns. However, using the full scene image as the background region for the background spectra calculation for each plume, similar to previous studies, the  $\Delta XCH_4$  of the plumes from the same point source showed large differences, especially for **Figure 3(f) and (g)**. The notable difference primarily arises from the different background used, suggesting the importance of selecting appropriate background regions. Note that the difference may also be slightly caused by the different signal noise ratio (SNR), as the plumes appear at different locations (at the bottom for (f) and at the top for (g)) of the imaging scene (**Figure D1**). As a result, they may be observed by different instrument detectors with different SNR that affect the detection accuracy of the plumes.





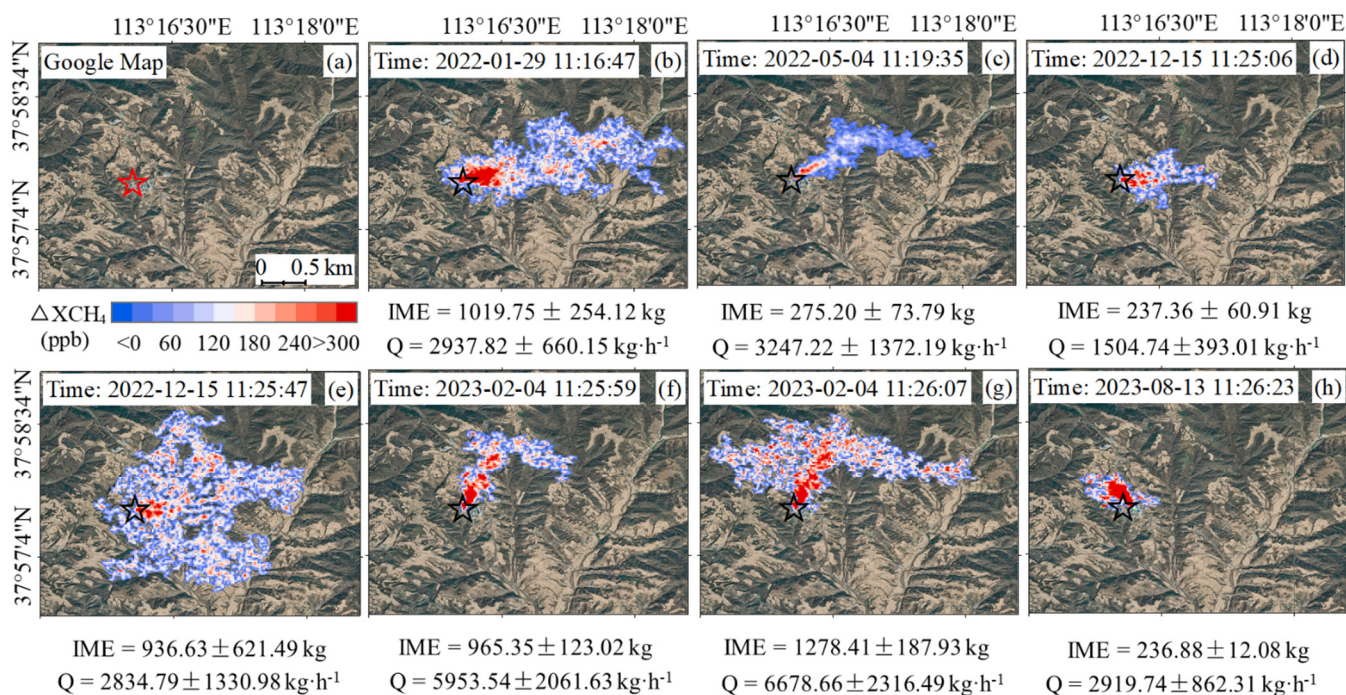
260

**Figure 3.** Example of  $\Delta XCH_4$  retrievals from one typical point source with multiple overpasses by GF-5B/AHSI, with its origin (Lat 37°57'36", Lon 113°16'04") marked with a red/black star. The detected plumes from the seven overpasses shown in (b)-(h). The observation times (in UTC+8 standard Beijing Time) are shown for each plume event, which are close to the local time. The background image in (a) is adopted from © Google Maps.

265

Based on the  $\Delta XCH_4$  retrieval and the flood-fill plume segmentation method, we obtained the plume characteristics and emission flux rate of the seven detections, as shown in **Figure 4**. The results indicate the following: (1) differences exist between the extracted plume features and visual segmentation. For instance, in **Figure 4(c)**, the elaborate plume automatically extracted using flood-fill would be challenged for manually drawing; (2) the point source emission flux rate varies between  $2834.79 \pm 1330.98 \text{ kg}\cdot\text{h}^{-1}$  in **Figure 4(e)** and  $6678.66 \pm 2316.49 \text{ kg}\cdot\text{h}^{-1}$  in **Figure 4(g)** (excluding incomplete observations in **Figure 4(d)**). Among these observations, four fall within a similar range between 2834.79 and 3247.22  $\text{kg}\cdot\text{h}^{-1}$ ; (3) the uncertainty of IME ranges from 5.07% to 66.38%, with the majority being below 30%, which is lower than the uncertainty caused by wind speed (~50%) in the emission flux rate calculation; (4) significant differences are evident in the plumes from adjacent detections of the same point source (e.g., **Figure 4(f)** and **(g)**), indicating the different backgrounds chosen for different imagery scenes are not optimal to monitoring the same emission plumes.

270



275

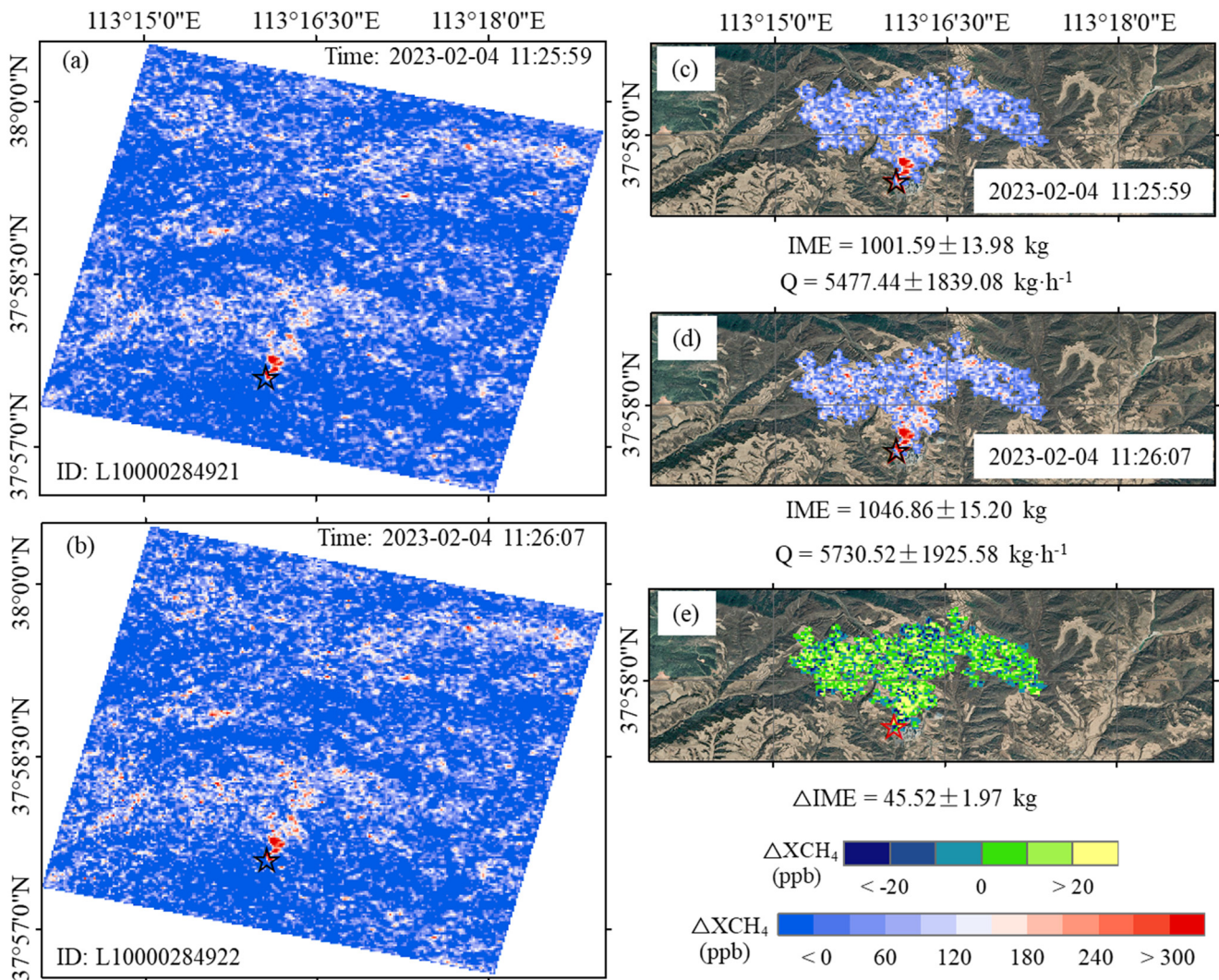
**Figure 4. Examples of extracted CH<sub>4</sub> point source, marked with red/black star (Lat 37°57'36''; Lon 113°16'04''), plume using flood-fill method based on the retrieved ΔXCH<sub>4</sub> maps, as shown in Figure 3, from a single point source with multiple overpasses by GF-5B/AHSI. The plume mass from IME model and the estimated emission flux rates are also indicated at the bottom of each map. The observation time in Beijing Time is shown for each plume event. All background images ((a) – (h)) are from © Google Maps.**

280

In order to eliminate the impact of background selection on estimating emission flux rate from the same point source, this study conducted a ΔXCH<sub>4</sub> retrieval experiment using overlapping area in the imagery maps of **Figure 3(f)** and **(g)** as the new background. The results based on the new backgrounds shown in **Figure 5** demonstrate highly similar ΔXCH<sub>4</sub> plume features between the two observations that are 8 seconds apart (**Figure 5(a)** and **(b)**). The extracted plume distribution and emission flux rate calculations shown in **Figure 5(c)** and **(d)** are almost identical. The integrated enhanced masses were 1001.59 ± 13.98 kg and 1046.86 ± 15.20 kg, respectively, with emission flux rates of 5477.44 ± 1839.08 kg·h<sup>-1</sup> and 5730.52 ± 1925.58 kg·h<sup>-1</sup>. This reduced estimation discrepancy between the two by 485.11 kg·h<sup>-1</sup> which is about 8.5% of the emission flux rate. Therefore, for the calculation of emissions for all plumes in Shanxi, we adopted a two-step approach to identify CH<sub>4</sub> plumes and estimate their emission rate. In step 1, the whole image is used to calculate ΔXCH<sub>4</sub> and identify plumes; In step 2, when implementing the flood-fill method using the strategy of selecting background regions as described in **Section 3.3.3**, the ΔXCH<sub>4</sub> is re-calculated using the same background regions for the flood-fill method. Therefore, the same background regions are used for calculating ΔXCH<sub>4</sub> using Equation 1, segmenting plumes using the flood-fill method, and estimating IME using Equation 2.

290





295 Figure 5.  $\Delta XCH_4$  retrievals from GF-5B/AHSI observations that are 8 seconds apart in (a) and (b) over the same point source, marked with red/black star (Lat 37°57'36"; Lon 113°16'04"). The retrievals are carried out using the same background region. The corresponding IME values and emission flux rates (Q) based on the extracted  $\Delta XCH_4$  maps are shown in (c) and (d), respectively. The difference between the two IME values is shown in (e). All background images ((c) – (e)) are from © Google Maps.

300 **4.2 Spatial distribution of point sources and their emission rates in Shanxi**

Based on the methods described above for estimating  $CH_4$  emission flux rate of point sources, we conducted a survey of all detectable point source emissions using all available imagery of GF-5B/AHSI from 2021 to 2023. In total, 93 point source plumes were identified. After averaging repetitive observations over the same point sources, a total of 32 point sources were identified, and their spatial distribution is depicted in **Figure 6**. **Figures 6(a)–(i)** exhibit typical plume extraction results around  
 305 three typical cities of Yangquan, Changzhi, and Jincheng. The emission flux rates range from  $2147.08 \pm 427.42$  to  $9198.03 \pm$

2059.18 kg·h<sup>-1</sup>. This result demonstrates a reasonably good consistency between the spatial locations of the actual CH<sub>4</sub> emission point sources identified in this study (red dots in **Figure 6**) and those extracted based on TROPOMI data (black dots in **Figure 6**), primarily concentrated around the three cities of Yangquan, Changzhi, and Jincheng. Given its high spatial resolution, the spatial locations derived from GF-5B/AHSI are expected to be more accurate. We found that the number of identified point sources is much fewer than those extracted from TROPOMI. This is primarily attributed to the much denser observations with daily global coverage and the different overpass time of TROPOMI (~13:30 local time). In addition, the high-resolution of the ΔXCH<sub>4</sub> retrieval results helped eliminate false positive signals due to surface interference elements like photovoltaic panels (further details are discussed in section 4.3.2) and greenhouse cultivation structures that are ubiquitous in Shanxi. Driven by wind speed and topography, different plumes from various point sources show distinctly varying dispersion distances, ranging from less than 1.0 km (e.g., **Figure 6(h)**) to 5.0 km (e.g., **Figure 6(d)**).

We further conducted IME calculations and emission flux rate estimations for the 93 plumes extracted from GF-5B/AHSI (**Figure 7(a)** and **(c)**). Additionally, based on multiple observations (from 2 to 8 times) of the same point source, we provided the highest and lowest emission flux rates and IME for the same point source (**Figure 7(b)** and **(d)**). The survey results revealed a diverse range of point source emission flux rates, varying from 761.78 ± 185.00 (minimum) to 12729.12 ± 4658.13 kg·h<sup>-1</sup> (maximum), with an average of approximately 4040.30 kg·h<sup>-1</sup>. The range of IME from point source emissions spans from 33.58 ± 6.27 (minimum) to 6587.50 ± 1925.31 kg (maximum). From the flux rate distribution in **Figure 7(a)** and the IME distribution in **Figure 7(c)**, we can see the order of IME does not strictly follow that of the flux rate for different point sources, suggesting contributions from the variability of wind conditions. Moreover, assuming a 50% uncertainty in U<sub>10</sub> (wind speed at 10-meter), in the uncertainty calculation of Q (emission flux rate), the impact of wind speed and IME uncertainties accounts for approximately 84.84% and 15.16%, respectively.

Furthermore, multiple observations of the same point source indicate significant variations in CH<sub>4</sub> emissions over time. The difference is as large as 10204.71 kg·h<sup>-1</sup>, which is about 7 times between the maximum and the minimum, as shown in **Figure 7(d)**. This difference suggests that a single observation does not adequately represent the overall or averaged emission scenario for any point source. Because the specific emission law of each emission point is unclear, and more coal mine emission time series detection experiments (**Qin et al., 2023**) are needed for the overall emission rate evaluation. Although, **Chen et al. (2022a)** used high density (26292 active wells) and highly repeated (115 flight days) measurements from aerial instrument to quantify methane emissions from the whole regional study area of New Mexico Permian Basin with persistence-averaged method. The persistent emission rate from a single point source was calculated with the emission detection probability derived from highly repeated observations. In this study, this may not be feasible, because the observations are too few to calculate the possibility of emission detection. The smallest emission rate of all the detected plumes, as shown in **Figure 7**, is 761.78 ± 185.00 kg·h<sup>-1</sup>, which is likely the detection limit of GF-5B AHSI based on our current method.



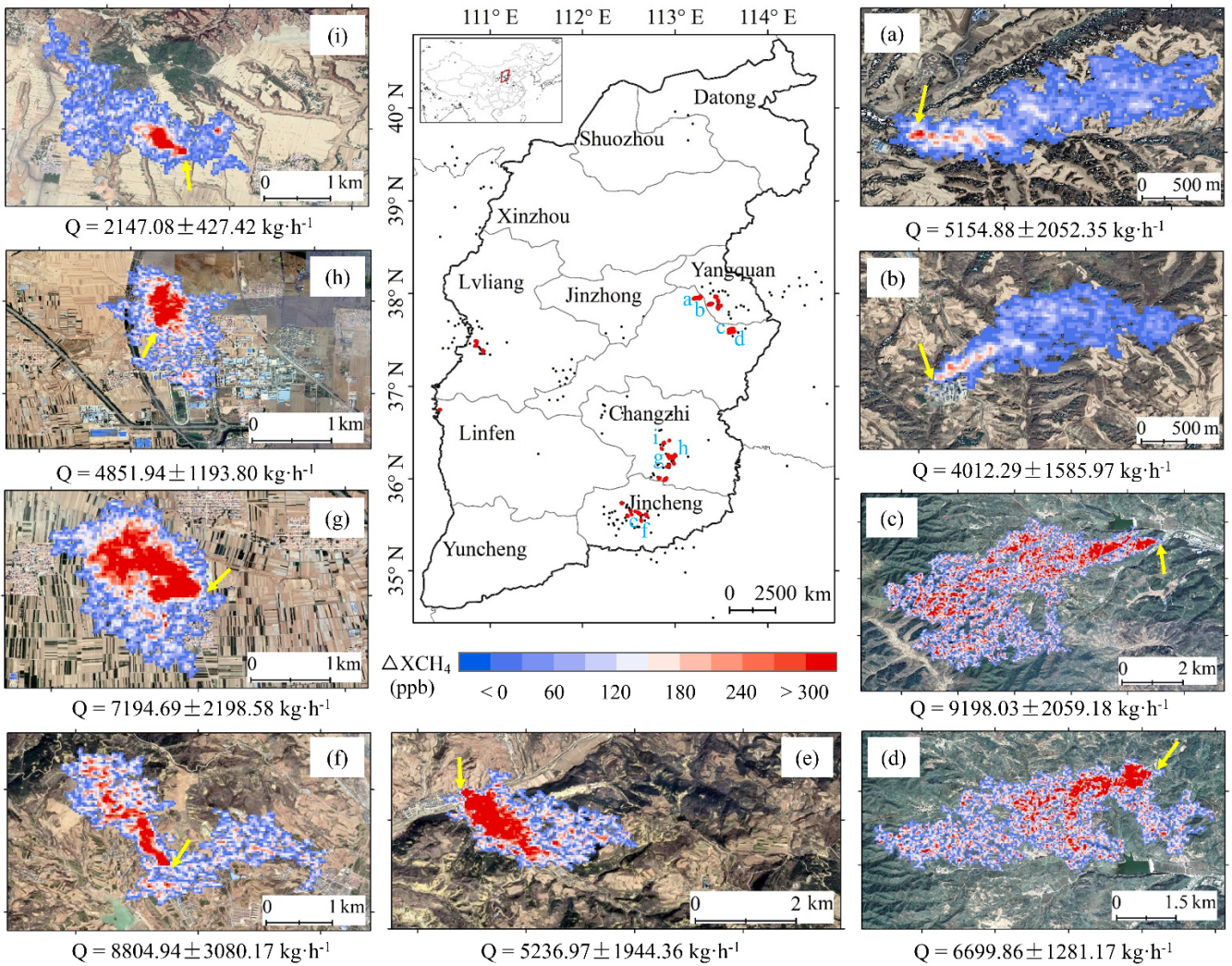
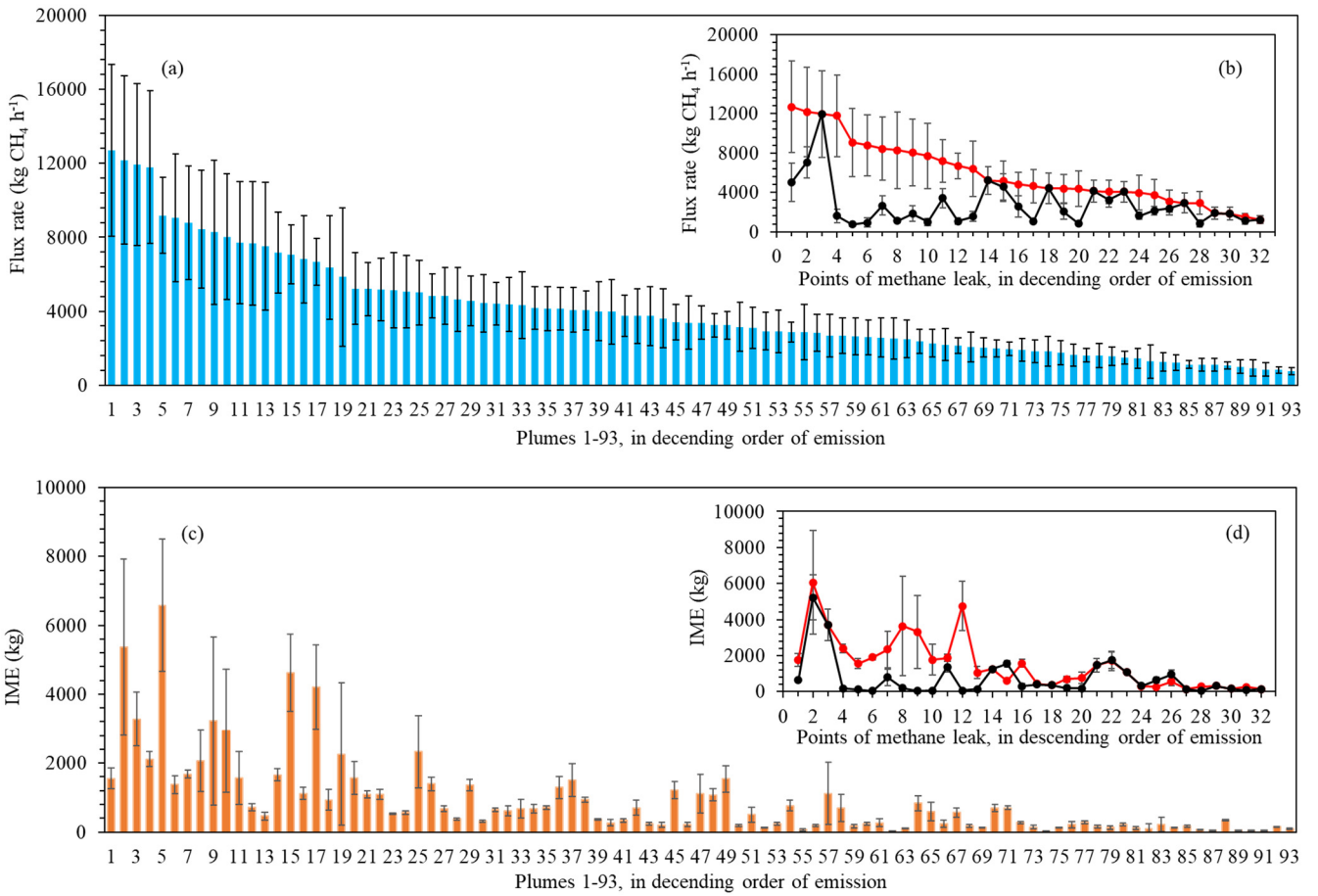


Figure 6. The spatial distribution of the identified CH<sub>4</sub> plumes (in red dots; in total of 93) in Shanxi using GF-5B/AHSI observations, as shown in the centre panel. The black dots represent the potential point sources detected by TROPOMI (Schuit et al., 2023). CH<sub>4</sub> plumes (a)-(i) are examples of the identified  $\Delta XCH_4$  plumes in Shanxi and the yellow arrow points to the origins of the identified point sources. All background images (a) – (i) are adopted from © Google Maps.

340



345 **Figure 7. (a) CH<sub>4</sub> emission flux rate from point source plumes #1-#93 in descending order of emissions, with the error bars representing the estimation uncertainty; (b) The maximum and minimum emission flux rates for each point source with more than 2 observations; (c) The corresponding IME estimates for plumes #1-#93 following the order in (a); (d) The maximum of minimum emission flux rates for each point source with more than 2 observations.**

## 350 4.3 Improvements on $\Delta XCH_4$ retrieval and emission flux rate estimation

### (1) Spectral calibration of GF-5B/AHSI observations

The impact of the wavelength shift and changes in FWHM of the spectral observations from GF-5B/AHSI on deriving  $\Delta XCH_4$  is demonstrated in **Figures 8 and 9**. **Figure 8** illustrates an example of the cross-track pixel variations of the estimated centre wavelength in (a) and FWHM in (b) in a single-scene image collected on 29 January 2022. The results reveal the distinct  
355 deviations from the nominal centre wavelength and FWHM among different track pixels during satellite imaging. **Figure 8(c)** displays the  $\Delta XCH_4$  of the corrected image, capturing plumes seen in **Figures 3(b), 6(c), and 6(d)**, among others. **Figures 8(d) and 8(e)** show the evident striping differences and spectral calibration's impact on calculating  $\Delta XCH_4$  of individual plume. The difference can reach up to 100 ppb. To further assess the spectral calibration's influence on  $CH_4$  point source estimation, this study analysed the shift in centre wavelength and changes in FWHM in 111 representative scenes with potential point  
360 source emissions using GF-5B/AHSI, as shown in **Figures 9(a) and 9(b)**. The results indicate that the average shift in centre wavelength of GF-5B/AHSI is approximately -0.05 nm, mostly ranging between -0.2 and 0.1 nm. The ratio of change in FWHM averages around 1.1, predominantly falling between 1.0 and 1.25 times (between 0-2.13 nm). Furthermore, the study evaluated the impact of spectral shift and FWHM change on the estimation of point source emission flux rate, as shown in **Figures 9(c) and 9(d)**. The results indicate that the caused difference of point source emission flux rate ranges from 0.43 to  
365 500.96  $kg \cdot h^{-1}$ . The average percentage of change is  $(1.78 \pm 1.39)\%$ . The maximum difference reaches up to about 5.0%. By considering the shift in central wavelength and change in FWHM in the spectral observations, it exhibits a potential to reduce the uncertainty of  $XCH_4$  emission rate estimation using GF-5B/AHSI.

### (2) Impact of heterogeneous surface features

Complex surface features significantly affect the identification of suspected point sources based on  $\Delta XCH_4$  maps and the  
370 derivation of point source emissions. In this study, we originally observed 219 instances of 113 suspicious point sources. In a more refined identification of these sources, we cross-checked and confirmed their positions using  $\Delta XCH_4$  retrievals from GF-5B/AHSI against high-resolution Google Earth imagery. Our findings revealed that the identification of point sources was significantly affected by the complex surfaces that exhibit strong SWIR absorption similar to  $CH_4$  and therefore result in false positive signal. Notably, array of solar panels that are widespread in Shanxi is the primary disruptor of the spectral matched  
375 filter retrieval method. An example of solar panel arrays is shown in **Figure 10**. Moreover, we found that surface features such as greenhouse structures, certain buildings, water bodies with plume-like distributions, and moist cultivated lands (like paddy fields) also generated noticeable high-value  $\Delta XCH_4$  interference signals. Therefore, in  $CH_4$  point source detection using GF-5B image, it's essential to consider combining with high resolution images to filter out false positive signals.

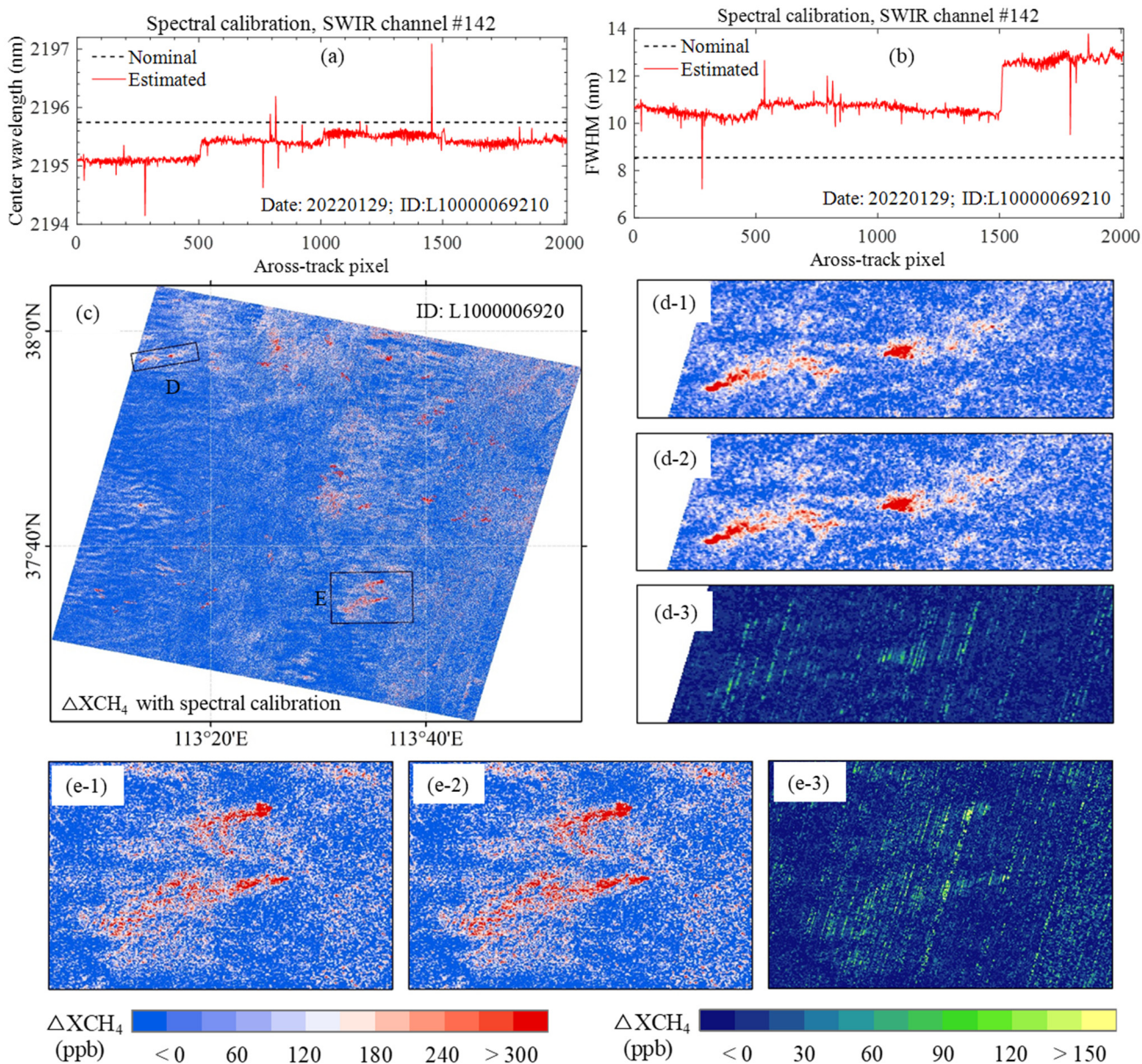
380

### (3) Evaluating wind fields from ERA5 reanalysis using observations from meteorological stations in Shanxi

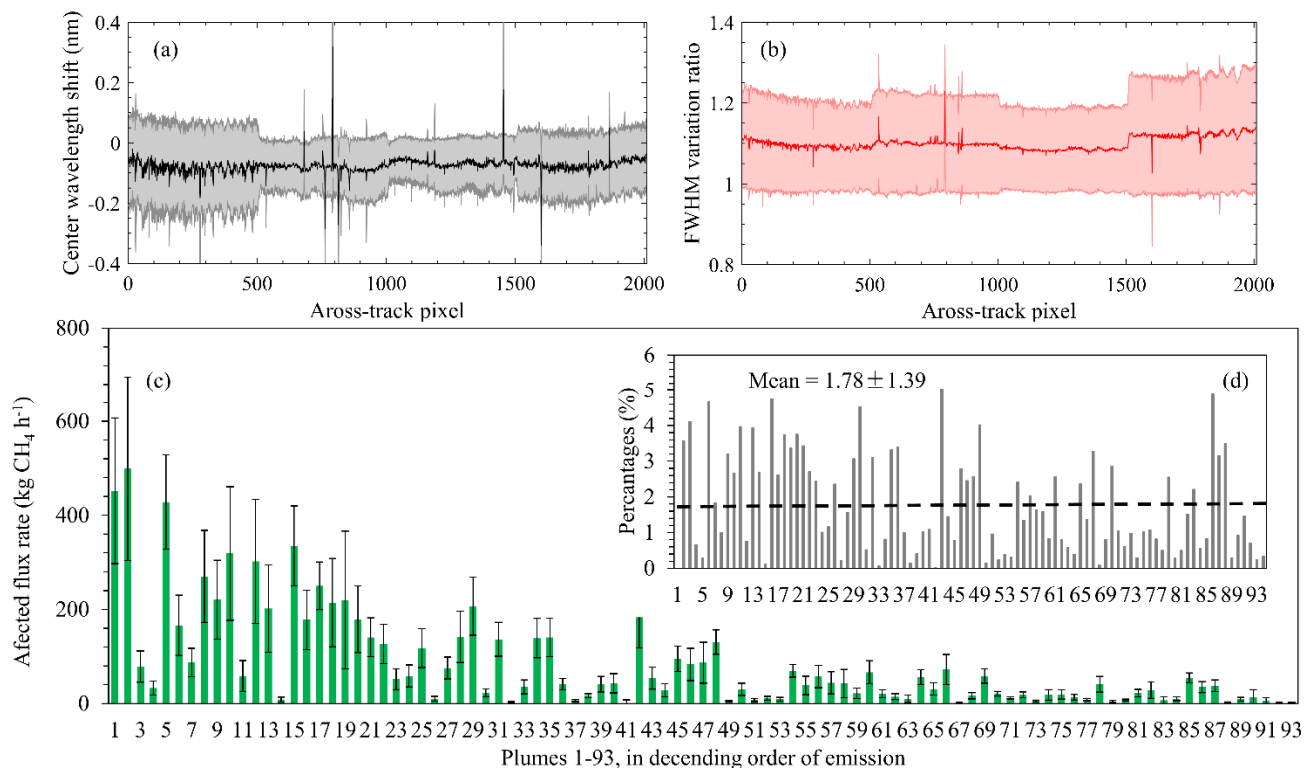
Wind fields, including wind speed and direction, are the primary drivers of uncertainty in estimating point source emissions, especially in plume segmentation and flux rate calculations. For plume segmentation, instead of visual interpretation, this study introduces the flood-fill method. Instead of searching for all possible directions in the current study, accurate wind direction information could enable us to precisely narrow down the flood-fill search directions, thereby removing abnormal signals from non-point source emissions, enhancing the reliability of plume segmentation. In emission flux rate estimation, aligning with previous studies, this study defined an uncertainty in ERA5 wind speed as 50%, thus leading to a significant uncertainty in the estimated emission rate. To evaluate the uncertainty of the wind fields from ERA5 reanalysis, which is widely used in many previous studies, this study compared them with data from three ground-based meteorological sites in Shanxi over the concentrated point source areas (**Figure 11**). The comparison results indicate that from 2021 to 2023, the overall bias in the ERA5 wind speed was approximately 1.30 m/s, which is close to 100% of bias on average. It has been recognized that the wind speed should be in a moderate range to allow detectable plumes from space. Too small wind speed may hamper the plume to develop, while too large wind speed may dilute the plume. It is observed in our cases that the wind speeds roughly fall within 0.5 to 2.5 m·s<sup>-1</sup> for most days with detectable point source plumes. If we assume this is the suitable wind speed range for satellite detection, as shown in black dots in the upper panel of **Figure 11**, the deviation is about 0.45-0.54 m·s<sup>-1</sup>, which is close to about 50% of the wind speed from ERA5. This uncertainty is consistent with the assumption of wind speed uncertainty (50%) in this study. In terms of wind direction, there are significant differences between ERA5 and the observations from meteorological sites. While ERA5 reanalysis data (at a height of 10-meter) show relatively constant wind direction, the measurements of wind direction from meteorological stations show a much larger range. This discrepancy indicates significant deviations between ERA5 reanalysis wind fields and actual wind conditions, challenging their direct application in point source plume identification and emission estimation. Consequently, leveraging high-density and high-precision meteorological observations from automatic meteorological monitoring stations, especially over regions with complex surface properties, could reduce the uncertainty and enhance the accuracy of satellite-based detection and estimation of CH<sub>4</sub> point source emissions.

However, a flat 50% wind error may underestimate uncertainty for small winds and overestimate uncertainty for large winds. Therefore, we carried out an evaluation of the plume emission uncertainty using the absolute wind error (1.297 m·s<sup>-1</sup> on average) estimated by comparing wind speeds from ERA5 and local meteorological stations in Shanxi. The results of CH<sub>4</sub> flux rates and their uncertainty are shown in **Figure E1**. As we expected, the uncertainty of flux decreased/increased at high/low wind speed, respectively. In addition, the impact of wind speed uncertainties accounts for approximately 86.31%, which is similar to the previous result based on a flat 50% wind error. This result supports the fact that wind speed remains the dominant factor contributing to the uncertainty in estimating CH<sub>4</sub> point source emissions.



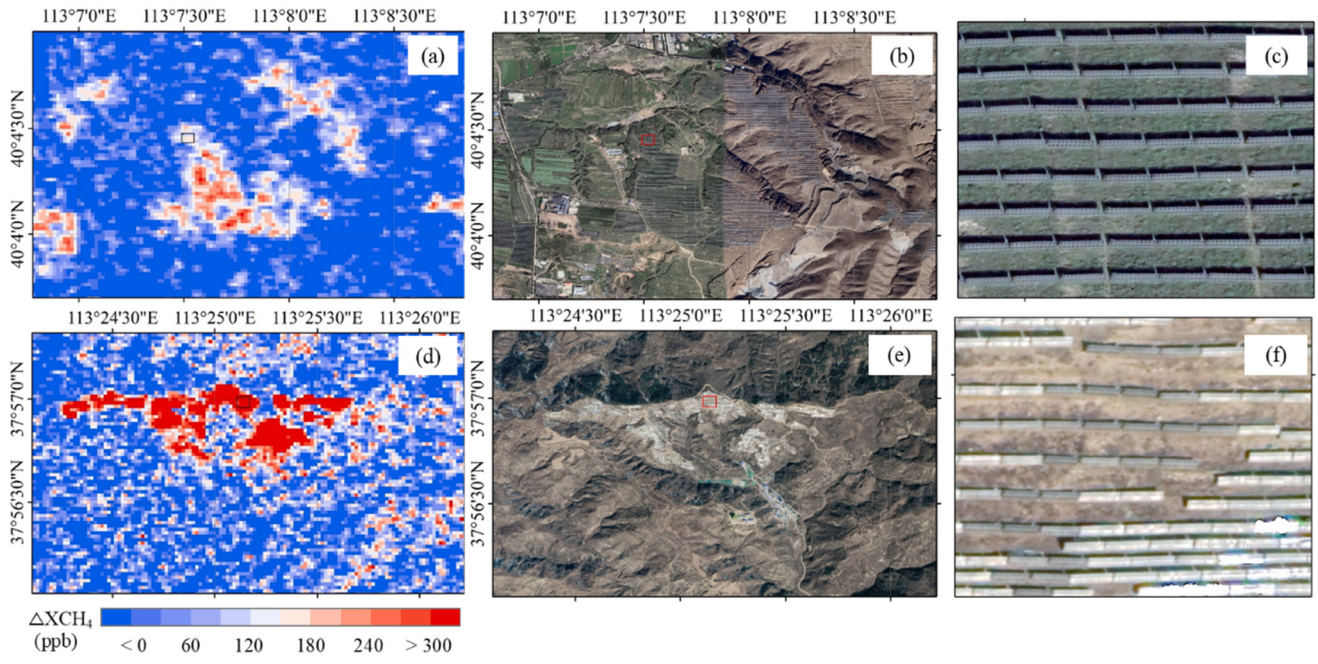


415 **Figure 8.** Example of the shift in centre wavelength and FWHM change for across-track pixels of channel #142 from GF-5B/AHSI SWIR imagery and their impacts for  $\Delta XCH_4$  retrieval. (a) shows the shift in centre wavelength for across-track pixels; (b) shows the FWHM variation ratio for across-track pixels; (c) shows the  $\Delta XCH_4$  retrieval of a single image with inputs of updated spectral calibration parameters; (d) and (e) are the comparison of zoom in plumes with and without inputs of updated spectral calibration parameters, in which (d-1) and (e-1) are results without calibration, and (d-2) and (e-2) are results with calibration, and (d-3) and (e-3) are the corresponding difference in  $\Delta XCH_4$  retrieval.



420 **Figure 9.** Statistics of the shift in centre wavelength in (a) and FWHM variation ratio in (b) of all 111 GF-5B/AHSI SWIR images with potential CH<sub>4</sub> point sources. The difference in the estimations of emission flux rates in (c) and corresponding difference in percentages in (d) for all detected CH<sub>4</sub> plumes shown in Figure 6 and Figure 7.





425

Figure 10. Examples of the impact of array of solar panels, which generates false positive signals, on the  $\Delta XCH_4$  retrieval in Shanxi.  $\Delta XCH_4$  retrievals with high values are similar to plume shapes in (a) and (d). These false positive signals are caused by the similar patterns of solar panel arrays, which can be seen from high resolution of google maps in (b) and (e). Zoom in details of solar panels in the red boxes in (b) and (e) can be found in (c) and (f), respectively.

430

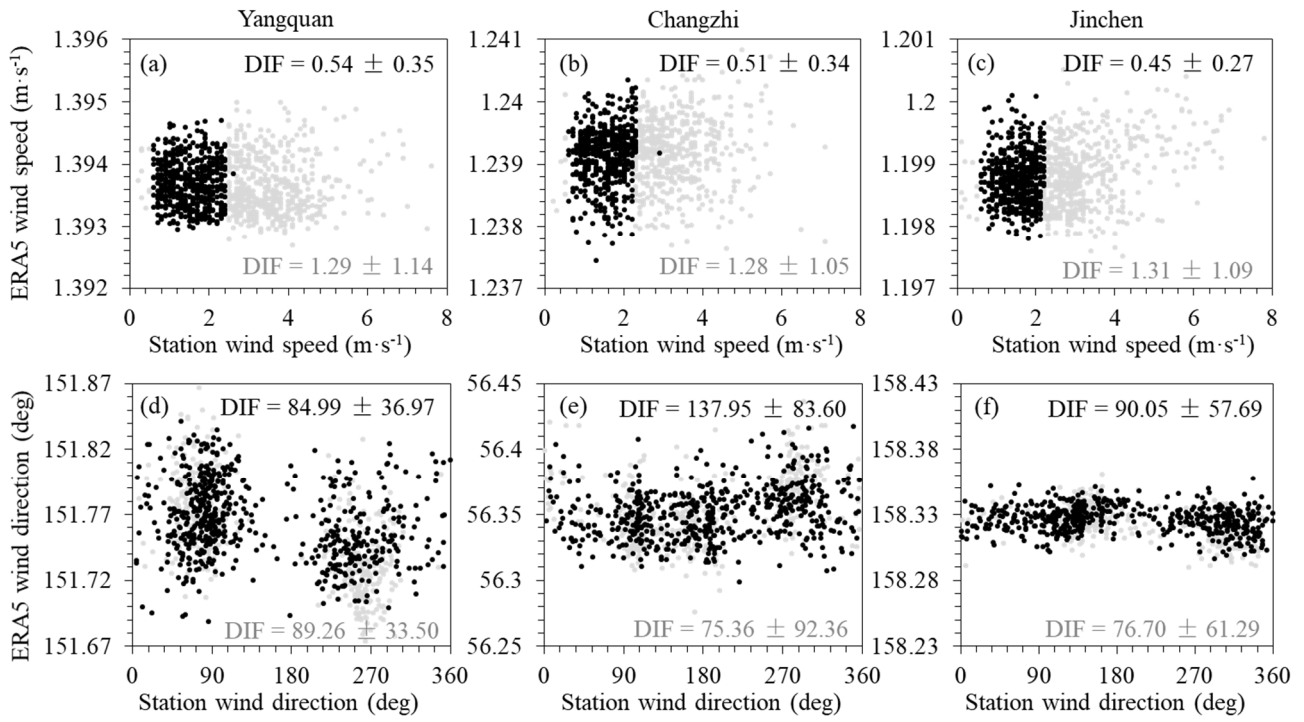


**Figure 11. Comparison of wind speeds (a-c) and directions (d-f) between ERA5 reanalysis and meteorological stations located in Yangquan, Changzhi and Jincheng cities in Shanxi, as indicated in Figure 1. Wind fields data from 2021 to 2023 are extracted in the daytime correspond to the GF-5B overpass time. Black dot data are selected according to the wind speed range of 0.5 to 2.5 m·s<sup>-1</sup>.**

## 5. Summary

In this study, we conducted a survey of CH<sub>4</sub> point sources emissions from coal mines in Shanxi, China using hyperspectral observations of GF-5B/AHSI. We first carried out the spectral calibration based on the estimates of the across-track changes in channel center wavelength and FWHM, which are approximately -0.05 nm and 10%, respectively. We adopted the widely used matched filter method to calculate the enhancement  $\Delta X_{CH_4}$ . Based on the enhancement, the emission plumes are extracted using the fill-flood method, which is an automated plume segmentation method. The emission flux rate and the associated uncertainty are eventually estimated using IME method. Our results show that the errors caused by spectral calibration (wavelength shift and FWHM change) and the selection of different background can reach up to 5.0% and 8.5%, respectively. Simultaneously, this study presents the spatial distribution and emission flux rates of 32 point sources and 93 observed plumes in Shanxi province from 2021 to 2023. The findings indicate that coal mine sources in Shanxi are primarily located around Yangquan, Changzhi, and Jincheng areas, with plume emission flux rates ranging from  $761.78 \pm 185.00$  (the minimum) to  $12729.12 \pm 4658.13$  kg·h<sup>-1</sup> (the maximum). Multiple repeated observations show significant differences in emission flux rates from the same source. The difference can reach to  $10204.71$  kg·h<sup>-1</sup> with a different by a factor of more than 7 times between the maximum and the minimum, indicating that a single overpass observation cannot represent the overall emissions of the point source. This study highlights that wind speed remains the primary factor contributing to uncertainty in point source emission estimation (approximately 84.84%), yet the uncertainty of IME (approximately 15.16%) is also important.

It is important to note that the plume shapes detected based solely on the  $\Delta X_{CH_4}$  maps contains false positive signals due to surface interference. The strong absorption in SWIR by certain surface types significantly disrupts point source detection and flux rate emissions. In the future, a fusion of hyperspectral spectra and multispectral image with high spatial resolution could effectively filter out false positive signals and remove surface covering interference. In addition, the uncertainty of wind field data remains significant sources of uncertainty in CH<sub>4</sub> point source emission flux rate estimation. From the evaluation of the accuracy of wind fields in ECMWF ERA5 reanalysis by comparing with ground-based meteorological station, we found large discrepancy, especially in wind directions. For regions with complex terrain like Shanxi, incorporating local meteorological measurements into the detection of CH<sub>4</sub> point source are important to achieve high accuracy.

**Data availability:**

465 Gaofen-5B AHSI images are downloaded from China Centre for Resources Satellite Data and Application, accessed from <https://data.cresda.cn/#/home>. Official applications are required for accessing the GF-5B/AHSI spectra. ERA5 reanalysis data from ECMWF can be accessed from <https://cds.climate.copernicus.eu/cdsapp#!/home>. Observations from national weather stations data are from China Meteorological Administration Data Centre, accessed from <http://data.cma.cn/en>. The dataset of detected plumes in Shanxi province of China during 2021-2023 using Gaofen-5B AHSI data will be made available upon publication.

**470 Author contributions:**

ZZ designed the study. ZH prepared all datasets, carried out the retrieval and result analysis. ZZ developed the retrieval codes. ZH wrote the first draft of the manuscript. LG and ML contributed to data acquisition and results analysis. All authors reviewed and proofread the manuscript.

**Acknowledgement:**

475 We thank Drs. L. Guanter, Y. Liu, and C. Sun for helpful discussions at the early stage of this work. This study was funded by the National Natural Science Foundation of Zhejiang Province (no. LQ21d050001) and the Research and development Project of “Jianbing” “Lingyan” of Zhejiang Province (no. 2023C03190). Z.-C. Zeng acknowledges funding from the National Natural Science Foundation of China (grant nos. 42275142 and no. 12292981). This work was also supported by High-performance Computing Platform of Peking University. We thank the support from the China Meteorological  
480 Administration Youth Innovation Team (Development and application of key technologies for greenhouse gas observation).

**Competing interests.**

The contact author has declared that none of the authors has any competing interests.

485

## References

- Chen, Y., Sherwin, E. D., Berman, E. S. F., Jones, B. B., Gordon, M. P., Wetherley, E. B., Kort, E. A., and Brandt, A. R.: Quantifying Regional Methane Emissions in the New Mexico Permian Basin with a Comprehensive Aerial Survey, *Environmental Science & Technology*, 56, 4317-4323, 10.1021/acs.est.1c06458, 2022a.
- 490 Chen, Z., Jacob, D. J., Nesser, H., Sulprizio, M. P., Lorente, A., Varon, D. J., Lu, X., Shen, L., Qu, Z., Penn, E., and Yu, X.: Methane emissions from China: a high-resolution inversion of TROPOMI satellite observations, *Atmospheric Chemistry and Physics*, 22, 10809-10826, 10.5194/acp-22-10809-2022, 2022b.
- Chen, Z., Jacob, D. J., Gautam, R., Omara, M., Stavins, R. N., Stowe, R. C., Nesser, H., Sulprizio, M. P., Lorente, A., Varon, D. J., Lu, X., Shen, L., Qu, Z., Pendergrass, D. C., and Hancock, S.: Satellite quantification of methane emissions and oil-gas
- 495 methane intensities from individual countries in the Middle East and North Africa: implications for climate action, *Atmospheric Chemistry and Physics*, 23, 5945-5967, 10.5194/acp-23-5945-2023, 2023.
- Cusworth, D. H., Duren, R. M., Thorpe, A. K., Tseng, E., Thompson, D., Guha, A., Newman, S., Foster, K. T., and Miller, C. E.: Using remote sensing to detect, validate, and quantify methane emissions from California solid waste operations, *Environmental Research Letters*, 15, 054012, 10.1088/1748-9326/ab7b99, 2020.
- 500 Duren, R. M., Thorpe, A. K., Foster, K. T., Rafiq, T., Hopkins, F. M., Yadav, V., Bue, B. D., Thompson, D. R., Conley, S., Colombi, N. K., Frankenberg, C., McCubbin, I. B., Eastwood, M. L., Falk, M., Herner, J. D., Croes, B. E., Green, R. O., and Miller, C. E.: California's methane super-emitters, *Nature*, 575, 180-184, 10.1038/s41586-019-1720-3, 2019.
- Ehret, T., De Truchis, A., Mazzolini, M., Morel, J.-M., D'asprenmont, A., Lauvaux, T., Duren, R., Cusworth, D., and Facciolo, G.: Global tracking and quantification of oil and gas methane emissions from recurrent sentinel-2 imagery, *Environmental*
- 505 *science & technology*, 56, 10517-10529, 2022.
- Farr, T. G., Rosen, P. A., Caro, E., Crippen, R., Duren, R., Hensley, S., Kobrick, M., Paller, M., Rodriguez, E., Roth, L., Seal, D., Shaffer, S., Shimada, J., Umland, J., Werner, M., Oskin, M., Burbank, D., and Alsdorf, D.: The Shuttle Radar Topography Mission, *Reviews of Geophysics*, 45, 10.1029/2005rg000183, 2007.
- Frankenberg, C., Thorpe, A. K., Thompson, D. R., Hulley, G., Kort, E. A., Vance, N., Borchardt, J., Krings, T., Gerilowski, K., Sweeney, C., Conley, S., Bue, B. D., Aubrey, A. D., Hook, S., and Green, R. O.: Airborne methane remote measurements reveal heavy-tail flux distribution in Four Corners region, *Proceedings of the National Academy of Sciences*, 113, 9734-9739, doi:10.1073/pnas.1605617113, 2016.
- Guanter, L., Segl, K., Sang, B., Alonso, L., Kaufmann, H., and Moreno, J.: Scene-based spectral calibration assessment of high spectral resolution imaging spectrometers, *Opt. Express*, 17, 11594-11606, 10.1364/OE.17.011594, 2009.

- 515 Guanter, L., Irakulis-Loitxate, I., Gorroño, J., Sánchez-García, E., Cusworth, D. H., Varon, D. J., Cogliati, S., and Colombo, R.: Mapping methane point emissions with the PRISMA spaceborne imaging spectrometer, *Remote Sensing of Environment*, 265, 112671, 10.1016/j.rse.2021.112671, 2021.
- Guanter, L., Kaufmann, H., Segl, K., Foerster, S., Rogass, C., Chabrillat, S., Kuester, T., Hollstein, A., Rossner, G., Chlebek, C., Straif, C., Fischer, S., Schrader, S., Storch, T., Heiden, U., Mueller, A., Bachmann, M., Mühle, H., Müller, R., Habermeyer, M., Ohndorf, A., Hill, J., Buddenbaum, H., Hostert, P., Van der Linden, S., Leitão, P. J., Rabe, A., Doerffer, R., Krasemann, H., Xi, H., Mauser, W., Hank, T., Locherer, M., Rast, M., Staenz, K., and Sang, B.: The EnMAP Spaceborne Imaging Spectroscopy Mission for Earth Observation, *Remote Sensing*, 7, 8830-8857, 2015.
- 520 He, Z., Lei, L., Welp, L., Zeng, Z.-C., Bie, N., Yang, S., and Liu, L.: Detection of Spatiotemporal Extreme Changes in Atmospheric CO<sub>2</sub> Concentration Based on Satellite Observations, *Remote Sensing*, 10, 839, 10.3390/rs10060839, 2018.
- 525 Huang, Y., Natraj, V., Zeng, Z. C., Kopparla, P., and Yung, Y. L.: Quantifying the impact of aerosol scattering on the retrieval of methane from airborne remote sensing measurements, *Atmos. Meas. Tech.*, 13, 6755-6769, 10.5194/amt-13-6755-2020, 2020.
- IPCC: Climate Change 2021: The Physical Science Basis, Contribution of Working Group I to the Sixth Assessment Report of the Intergovernmental Panel on Climate Change, Cambridge University Press, Cambridge, UK and New York, NY, USA, 10.1017/9781009157896, 2021.
- 530 Irakulis-Loitxate, I., Guanter, L., Liu, Y.-N., Varon, D. J., Maasackers, J. D., Zhang, Y., Chulakadabba, A., Wofsy, S. C., Thorpe, A. K., and Duren, R. M.: Satellite-based survey of extreme methane emissions in the Permian basin, *Science advances*, 7, eabf4507, 2021.
- Jacob, D. J., Varon, D. J., Cusworth, D. H., Dennison, P. E., Frankenberg, C., Gautam, R., Guanter, L., Kelley, J., McKeever, J., Ott, L. E., Poulter, B., Qu, Z., Thorpe, A. K., Worden, J. R., and Duren, R. M.: Quantifying methane emissions from the global scale down to point sources using satellite observations of atmospheric methane, *Atmospheric Chemistry and Physics*, 22, 9617-9646, 10.5194/acp-22-9617-2022, 2022.
- 535 Jervis, D., McKeever, J., Durak, B. O. A., Sloan, J. J., Gains, D., Varon, D. J., Ramier, A., Strupler, M., and Tarrant, E.: The GHGSat-D imaging spectrometer, *Atmospheric Measurement Techniques*, 14, 2127-2140, 10.5194/amt-14-2127-2021, 2021.
- 540 Jongaramrungruang, S., Matheou, G., Thorpe, A. K., Zeng, Z. C., and Frankenberg, C.: Remote sensing of methane plumes: instrument tradeoff analysis for detecting and quantifying local sources at global scale, *Atmos. Meas. Tech.*, 14, 7999-8017, 10.5194/amt-14-7999-2021, 2021.
- Lauvaux, T., Giron, C., Mazzolini, M., d'Aspremont, A., Duren, R., Cusworth, D., Shindell, D., and Ciais, P.: Global assessment of oil and gas methane ultra-emitters, *Science*, 375, 557-561, 2022.

- 545 Li, F., Sun, S., Zhang, Y., Feng, C., Chen, C., Mao, H., and Liu, Y.: Mapping methane super-emitters in China and United States with GF5-02 hyperspectral imaging spectrometer, *National Remote Sensing Bulletin*, 0, 1-15, 10.11834/jrs.20232453, 2023.
- Liu, Q., Yu, T., and Zhang, W.: Validation of GaoFen-1 Satellite Geometric Products Based on Reference Data, *Journal of the Indian Society of Remote Sensing*, 47, 1331-1346, 10.1007/s12524-019-01017-2, 2019a.
- 550 Liu, Y.-N., Sun, D.-X., Hu, X.-N., Ye, X., Li, Y.-D., Liu, S.-F., Cao, K.-Q., Chai, M.-Y., Zhang, J., and Zhang, Y.: The advanced hyperspectral imager: aboard China's GaoFen-5 satellite, *IEEE Geoscience and Remote Sensing Magazine*, 7, 23-32, 2019b.
- Lu, X., Jacob, D. J., Wang, H., Maasakkers, J. D., Zhang, Y., Scarpelli, T. R., Shen, L., Qu, Z., Sulprizio, M. P., Nesser, H., Bloom, A. A., Ma, S., Worden, J. R., Fan, S., Parker, R. J., Boesch, H., Gautam, R., Gordon, D., Moran, M. D., Reuland, F.,
- 555 Villasana, C. A. O., and Andrews, A.: Methane emissions in the United States, Canada, and Mexico: evaluation of national methane emission inventories and 2010–2017 sectoral trends by inverse analysis of in situ (GLOBALVIEWplus CH<sub>4</sub> ObsPack) and satellite (GOSAT) atmospheric observations, *Atmospheric Chemistry and Physics*, 22, 395-418, 10.5194/acp-22-395-2022, 2022.
- Miller, S. M., Michalak, A. M., Detmers, R. G., Hasekamp, O. P., Bruhwiler, L. M. P., and Schwietzke, S.: China's coal mine methane regulations have not curbed growing emissions, *Nature communications*, 10, 10.1038/s41467-018-07891-7, 2019.
- 560 Muñoz-Sabater, J., Dutra, E., Agustí-Panareda, A., Albergel, C., Arduini, G., Balsamo, G., Boussetta, S., Choulga, M., Harrigan, S., and Hersbach, H.: ERA5-Land: A state-of-the-art global reanalysis dataset for land applications, *Earth system science data*, 13, 4349-4383, 2021.
- Pandey, S., Houweling, S., Lorente, A., Borsdorff, T., Tsvilidou, M., Bloom, A. A., Poulter, B., Zhang, Z., and Aben, I.: Using satellite data to identify the methane emission controls of South Sudan's wetlands, *Biogeosciences*, 18, 557-572, 10.5194/bg-18-557-2021, 2021.
- 565 Qin, K., Hu, W., He, Q., Lu, F., and Cohen, J. B.: Individual Coal Mine Methane Emissions Constrained by Eddy-Covariance Measurements: Low Bias and Missing Sources, *EGU sphere*, 2023, 1-49, 10.5194/egusphere-2023-1210, 2023.
- Sánchez-García, E., Gorroño, J., Irakulis-Loitxate, I., Varon, D. J., and Guanter, L.: Mapping methane plumes at very high spatial resolution with the WorldView-3 satellite, *Atmospheric Measurement Techniques*, 15, 1657-1674, 10.5194/amt-15-1657-2022, 2022.
- 570 Saunio, M., Stavert, A. R., Poulter, B., Bousquet, P., Canadell, J. G., Jackson, R. B., Raymond, P. A., Dlugokencky, E. J., Houweling, S., Patra, P. K., Ciais, P., Arora, V. K., Bastviken, D., Bergamaschi, P., Blake, D. R., Brailsford, G., Bruhwiler, L., Carlson, K. M., Carrol, M., Castaldi, S., Chandra, N., Crevoisier, C., Crill, P. M., Covey, K., Curry, C. L., Etiope, G.,
- 575 Frankenberg, C., Gedney, N., Hegglin, M. I., Höglund-Isaksson, L., Hugelius, G., Ishizawa, M., Ito, A., Janssens-Maenhout,

- G., Jensen, K. M., Joos, F., Kleinen, T., Krummel, P. B., Langenfelds, R. L., Laruelle, G. G., Liu, L., Machida, T., Maksyutov, S., McDonald, K. C., McNorton, J., Miller, P. A., Melton, J. R., Morino, I., Müller, J., Murguía-Flores, F., Naik, V., Niwa, Y., Noce, S., O'Doherty, S., Parker, R. J., Peng, C., Peng, S., Peters, G. P., Prigent, C., Prinn, R., Ramonet, M., Regnier, P., Riley, W. J., Rosentreter, J. A., Segers, A., Simpson, I. J., Shi, H., Smith, S. J., Steele, L. P., Thornton, B. F., Tian, H., Tohjima, Y.,  
580 Tubiello, F. N., Tsuruta, A., Viovy, N., Voulgarakis, A., Weber, T. S., van Weele, M., van der Werf, G. R., Weiss, R. F., Worthy, D., Wunch, D., Yin, Y., Yoshida, Y., Zhang, W., Zhang, Z., Zhao, Y., Zheng, B., Zhu, Q., Zhu, Q., and Zhuang, Q.: The Global Methane Budget 2000–2017, *Earth System Science Data*, 12, 1561-1623, 10.5194/essd-12-1561-2020, 2020.
- Schuit, B. J., Maasackers, J. D., Bijl, P., Mahapatra, G., van den Berg, A.-W., Pandey, S., Lorente, A., Borsdorff, T., Houweling, S., Varon, D. J., McKeever, J., Jervis, D., Girard, M., Irakulis-Loitxate, I., Gorroño, J., Guanter, L., Cusworth, D. H., and Aben,  
585 I.: Automated detection and monitoring of methane super-emitters using satellite data, *Atmospheric Chemistry and Physics*, 23, 9071-9098, 10.5194/acp-23-9071-2023, 2023.
- Thompson, D. R., Thorpe, A. K., Frankenberg, C., Green, R. O., Duren, R., Guanter, L., Hollstein, A., Middleton, E., Ong, L., and Ungar, S.: Space-based remote imaging spectroscopy of the Aliso Canyon CH<sub>4</sub> superemitter, *Geophysical Research Letters*, 43, 6571-6578, 10.1002/2016gl069079, 2016.
- 590 Thorpe, A. K., Green, R. O., Thompson, D. R., Brodrick, P. G., Chapman, J. W., Elder, C. D., Irakulis-Loitxate, I., Cusworth, D. H., Ayasse, A. K., Duren, R. M., Frankenberg, C., Guanter, L., Worden, J. R., Dennison, P. E., Roberts, D. A., Chadwick, K. D., Eastwood, M. L., Fahlen, J. E., and Miller, C. E.: Attribution of individual methane and carbon dioxide emission sources using EMIT observations from space, *Science advances*, 9, eadh2391, doi:10.1126/sciadv.adh2391, 2023.
- Varon, D. J., Jervis, D., McKeever, J., Spence, I., Gains, D., and Jacob, D. J.: High-frequency monitoring of anomalous  
595 methane point sources with multispectral Sentinel-2 satellite observations, *Atmospheric Measurement Techniques*, 14, 2771-2785, 10.5194/amt-14-2771-2021, 2021.
- Varon, D. J., Jacob, D. J., McKeever, J., Jervis, D., Durak, B. O. A., Xia, Y., and Huang, Y.: Quantifying methane point sources from fine-scale satellite observations of atmospheric methane plumes, *Atmospheric Measurement Techniques*, 11, 5673-5686, 10.5194/amt-11-5673-2018, 2018.
- 600 Varon, D. J., McKeever, J., Jervis, D., Maasackers, J. D., Pandey, S., Houweling, S., Aben, I., Scarpelli, T., and Jacob, D. J.: Satellite Discovery of Anomalously Large Methane Point Sources From Oil/Gas Production, *Geophysical Research Letters*, 46, 13507-13516, 10.1029/2019gl083798, 2019.
- Zeng, Z., Natraj, V., Xu, F., Chen, S., Gong, F.-Y., Pongetti, T. J., Sung, K., Toon, G. C., Sander, S. P., and Yung, Y. L.: GFIT3: A full physics retrieval algorithm for remote sensing of greenhouse gases in the presence of aerosols, *Atmospheric  
605 Measurement Techniques*, 2021.



Zheng, C., Jiang, B., Xue, S., Chen, Z., and Li, H.: Coalbed methane emissions and drainage methods in underground mining for mining safety and environmental benefits: A review, *Process Safety and Environmental Protection*, 127, 103-124, <https://doi.org/10.1016/j.psep.2019.05.010>, 2019.

Zscheischler, J., Mahecha, M. D., Harmeling, S., and Reichstein, M.: Detection and attribution of large spatiotemporal extreme events in Earth observation data, *Ecological Informatics*, 15, 66-73, [10.1016/j.ecoinf.2013.03.004](https://doi.org/10.1016/j.ecoinf.2013.03.004), 2013.

## Appendix A: Geometric localization of GF-5B/AHSI images

The identification of CH<sub>4</sub> point sources using high-resolution satellite imagery is closely linked to land cover, while the accurate calculation of ΔXCH<sub>4</sub> is significantly affected by spectral differences in the background within the study area. Hence, precise geometric localization (Equations 4–6) of the GF-5B satellite images is crucial. The retrieval of ΔXCH<sub>4</sub> involves both forward and inverse computations of the Rational Polynomial Coefficients (RPCs) in high-resolution imagery (Liu et al., 2019). The forward computation entails transforming the row and column indices ( $Row_i, Col_i$ ) of the image data into geographical coordinates ( $Lat_i, Lon_i$ ), aiding in detecting and identifying ΔXCH<sub>4</sub> point sources. Conversely, the reverse computation aims to optimize background concentration calculations by transforming detected point source geographical coordinates back to the image's row and column indices.

$$\begin{cases} Row_i = F_a(U_i, V_i, W)/F_b(U_i, V_i, W_i) \\ Col_i = F_c(U_i, V_i, W)/F_d(U_i, V_i, W_i) \end{cases} \quad (4)$$

$$F_a(U, V, W) = a_1 + a_2V + a_3U + a_4W + a_5VU + a_6VW + a_7UW + a_8V^2 + a_9U^2 + a_{10}W^2 + a_{11}UVW + a_{12}V^3 + a_{13}VU^2 + a_{14}VW^2 + a_{15}V^2U + a_{16}V^3 + a_{17}UW^2 + a_{18}V^2W + a_{19}U^2W + a_{20}W^3 \quad (5)$$

$$\begin{cases} U_i = (Lat_i - Lat\_off)/Lat\_scale \\ V_i = (Lon_i - Lon\_off)/Lon\_scale \\ W_i = (Height_i - Heigh\_off)/Heigh\_scale \end{cases} \quad (6)$$

where,  $a_1 \dots a_{20}$ ,  $b_1 \dots b_{20}$ ,  $c_1 \dots c_{20}$ ,  $d_1 \dots d_{20}$ ,  $Lat\_off$ ,  $Lat\_scale$ ,  $Lon\_off$ ,  $Lon\_scale$ ,  $Heigh\_off$  and  $Heigh\_scale$  are rational polynomial coefficients (RPCs), which can be obtained from incidental data of the GF-5B images.

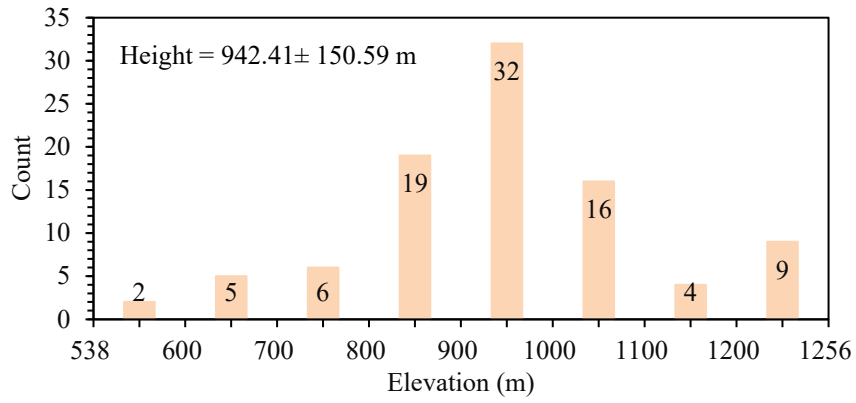


Figure B1. Histogram of the elevation for the detected plumes in Shanxi. The elevation data is from the DEM shown in Section 2.3.

Appendix C: Examples of plume segmentation using flood-fill method with different input parameters

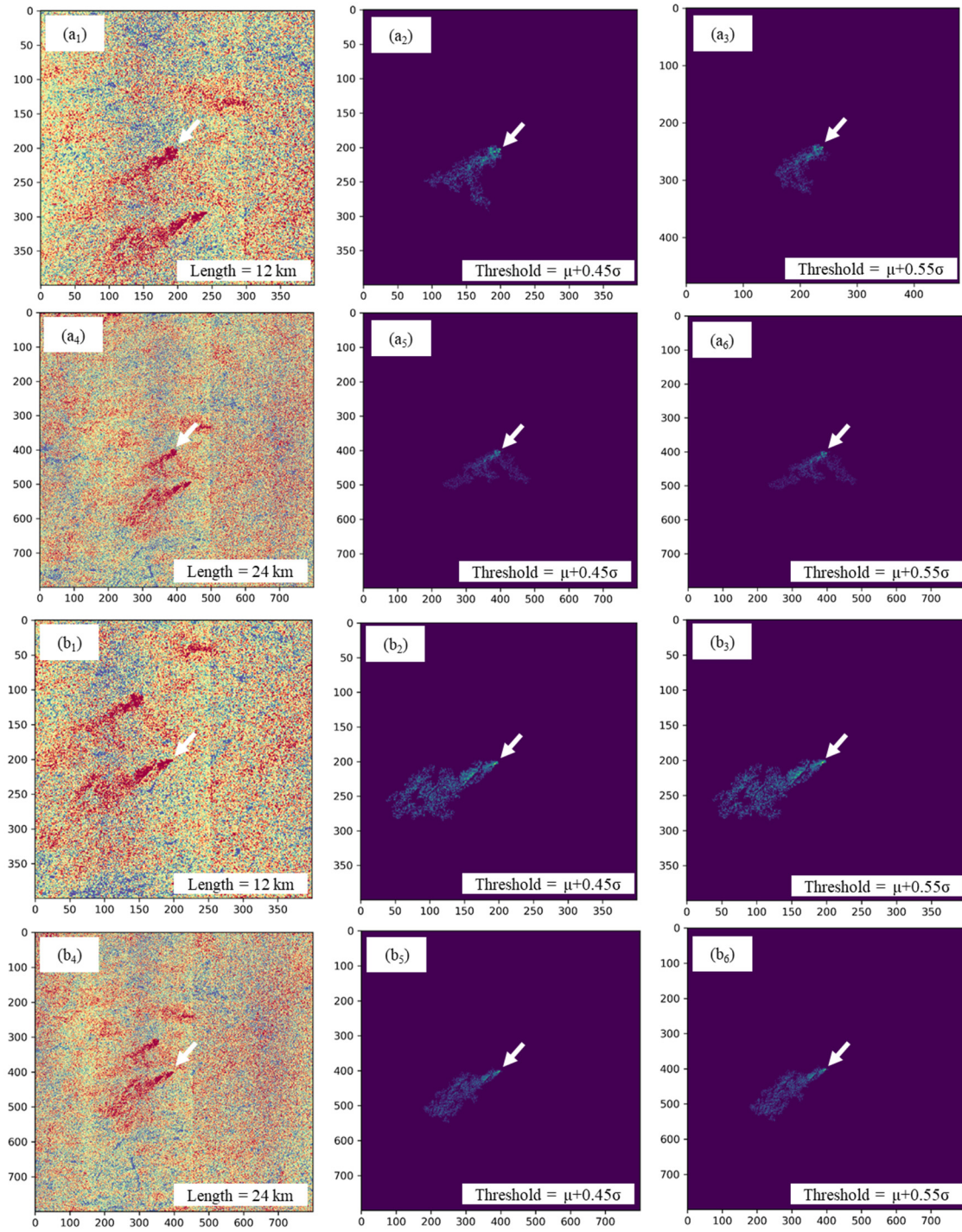
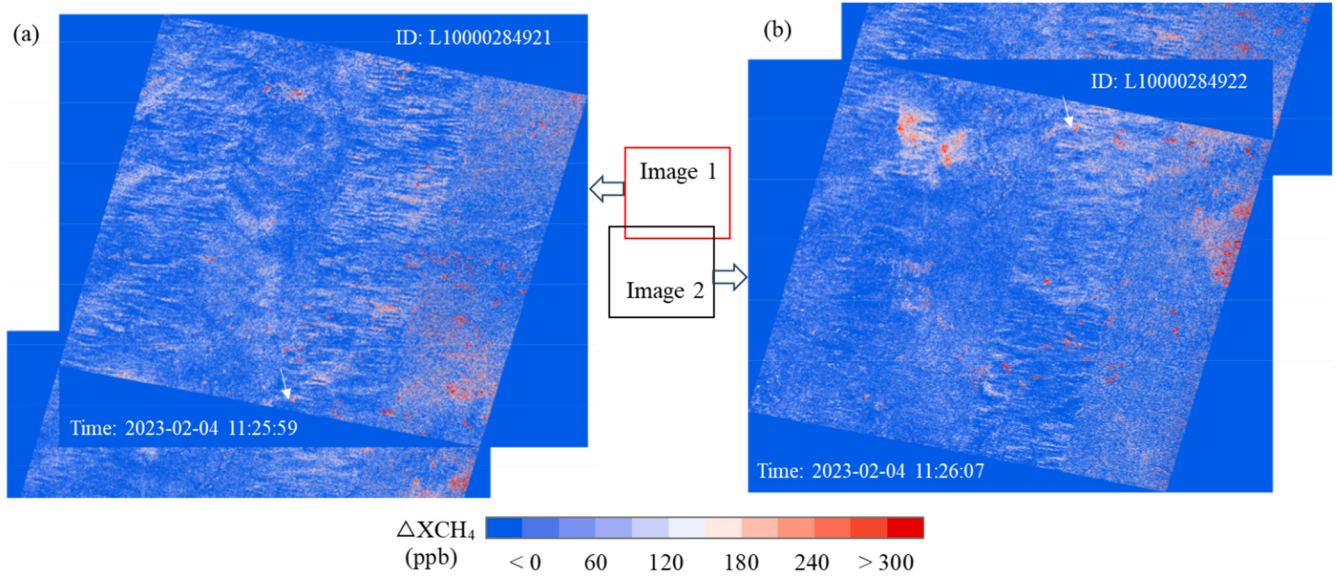


Figure C1. Examples of plume segmentation in flood-fill method using different lengths for the background square and different segmentation thresholds. Two plumes are given in  $a_1$ - $a_6$  and  $b_1$ - $b_6$  as examples, in which  $a_1$ - $a_3$  and  $b_1$ - $b_3$  are for the length of 12 km and  $a_4$ - $a_6$  and  $b_4$ - $b_6$  are for the length of 24 km. Two different thresholds,  $\mu+0.45\sigma$  and  $\mu+0.55\sigma$ , are given for the two plume examples.

640

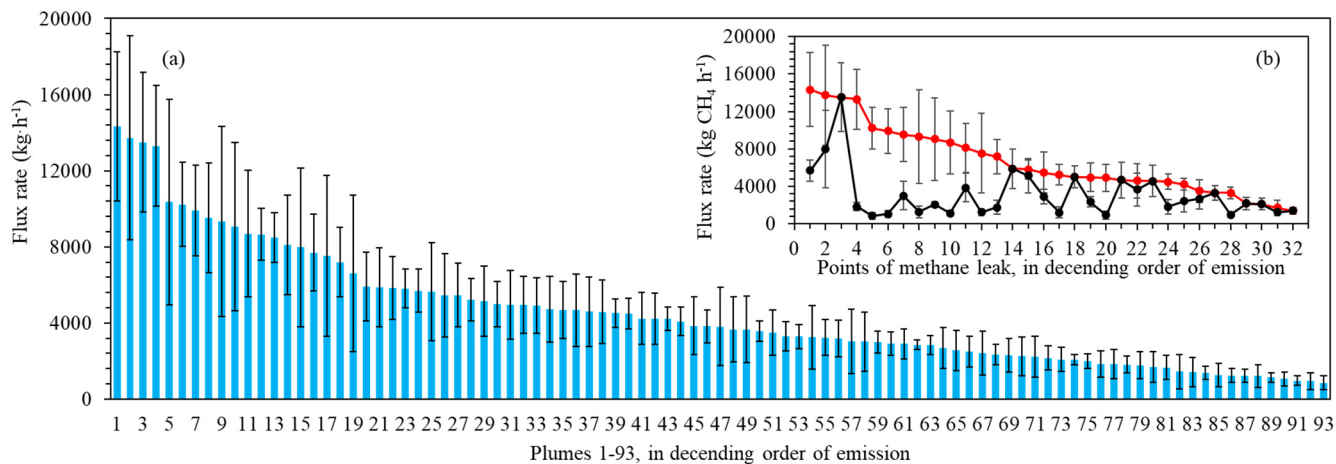
**Appendix D: An example of the same plume target inside the nearest two full images**



**Figure D1. The full images of  $\Delta XCH_4$  for Figure 3f (a) and Figure 3g (b). The plume target (pointed by the white arrow) appears in the overlapping region of the two images.**

645

**Appendix E: CH<sub>4</sub> emission flux rates from point source plumes in Shanxi with an absolute wind speed uncertainty estimated by comparing wind speeds from EAR5 and local meteorological stations**



650 **Figure E1. Uncertainty of CH<sub>4</sub> emission flux rates using an absolute wind speed uncertainty. (a) CH<sub>4</sub> emission flux rates from point source plumes #1-#93 in descending order of emissions, with the error bars representing the estimation uncertainty. The uncertainty of the wind speed (1.297 m·s<sup>-1</sup>) is estimated by comparing wind speeds from EAR5 and local meteorological stations, as described in Section 4.3.3; (b) The maximum and minimum emission flux rates for each point source with more than 2 observations.**